Project THEMIS

Technical Report No. 15

INTERACTION OF A WALL-JET WITH A SHEAR FLOW

by

S. Mukherji* and W. Z. Sadeh**

Fluid Dynamics and Diffusion Laboratory
Fluid Mechanics Program
Department of Civil Engineering
Colorado State University
Fort Collins, Colorado

Prepared for
Office of Naval Research
Contract No. N00014-68-A-0493-0001.
Project No. NR 062-414/6-6-68(Code 438)
U. S. Department of Defense
Washington, D. C.

March 1972 CER70-71SM-WZS82

* Research Assistant.
** Associate Professor of Engineering.

ACKNOWLEDGEMENTS

The support of this work by project THEMIS under the supervision of Mr. R. D. Cooper (Fluid Dynamics Branch, Office of Naval Research, Contract N00014-68-A-0493-0001) is gratefully acknowledged.

ABSTRACT

An experimental investigation of a flow field resulting from the interaction between a spreading turbulent wall jet on a smooth surface and a shear flow was conducted. The combined flow was formed by a downward circular jet penetrating perpendicularly a moving shear stream confined within a constant-area open channel. A hot-wire survey of mean velocity and turbulence intensity was carried out.

A similar variation of mean velocity was found to exist on either side of the axis of the impinging jet, provided that appropriate characteristic scales were used. Similarity was obtained by dividing the flow into an inner and an outer layer, and by subdividing the latter into two zones of equal thickness. This partition into three distinct regions was deduced from the velocity change with height and, particularly, from the existence of a local characteristic maximum velocity. Within each region, velocity and length scales were formulated. The former was defined in terms of the local maximum velocity for the inner layer. In the two zones of the outer layer the velocity scales were defined in terms of the zonal maximum excess velocities. The excess velocity was computed with respect to the local free-stream velocity characteristic to this flow. In all three regions, the thicknesses of the layers were utilized as the length scale. The similarity in mean velocity variation is corroborated by the computed constant values of the shape factor for each particular region of the flow.

The use of analogous scales led to similarity in the change of mean energy. Furthermore, it was found that the turbulence intensity variation exhibited similarity when the same scales used for the velocity were employed.

LIST OF SYMBOLS

A	constant of proportionality
a,b	wall-jet similarity exponents
B	half-width of shear flow channel
d	hot-wire diameter
E	actual voltage drop across the hot-wire placed in a flow; Eq. (4.1)
E_o	voltage drop across the hot-wire placed in still air; Eq. (4.1)
E	total longitudinal kinetic energy per unit mass and per unit area of flow; Eq. (5.1)
E	mean local kinetic energy per unit mass; Eq. (5.15)
ΔE	mean local excess kinetic energy; Eqs. (5.16) and (5.17)
e	fluctuating voltage
H	shape factor
h	jet orifice distance from the flat surface
l	hot-wire length
n	exponent
R	jet orifice radius
Re_δ	Reynolds number based on boundary-layer thickness
Re_x	Reynolds number based on downstream distance
T_u	longitudinal turbulence intensity
U	mean velocity along x-axis
U_m	maximum velocity corresponding to height δ_m
U_o	free-stream velocity
U_1	mean velocity corresponding to height δ_1
U_2	mean velocity corresponding to height δ_2

ΔU	excess velocity defined by Eq. (5.2)
ΔU_m	maximum excess velocity defined by Eq. (5.3)
ΔU_1	excess velocity in Zone II defined by Eq. (5.4)
u	fluctuating velocity in the x-direction
V	mean velocity along y-axis
W_o	jet efflux velocity
W	mean velocity along z-axis
x,y,z	cartesian coordinates
α	wall-jet similarity parameter
Δ	displacement thickness
δ	boundary-layer thickness
δ_m	inner-layer thickness
δ_t	outer-layer thickness (characteristic jet thickness or jet width)
δ_1	height corresponding to the outer edge of Zone I
δ_2	total boundary-layer thickness
ζ	dimensionless excess height in outer layer
θ	momentum thickness
ν	kinematic viscosity
ρ	density
ψ	dimensionless excess velocity in outer layer

Superscripts

*	means "having dimensions"
$\overline{\ }$	means time-averaged

Subscripts

c	combined flow
i,k,ℓ	indices

j	wall jet
m	inner layer
s	shear flow
rms	root-mean-square
1	Zone I
2	Zone II

LIST OF FIGURES

TABLE OF CONTENTS

1. INTRODUCTION

The interaction of a turbulent jet with a shear flow exhibits numerous interesting flow features and has many practical applications. Besides causing significant variations of the mean velocity of both flows, the interaction produces large-scale eddies, high levels of turbulence and, often, flow reversals. In the atmosphere, interaction of low level jet streams with the atmospheric boundary layer results in strongly perturbed wind profiles. Changes in wind variation affect the maneuverability of aircraft, missile launching, parachute deployment of men and materials, entrainment of debris, jet blasting and so forth. Operation of V/STOL aircrafts and Ground Effect Machines (GEM) represent further examples of disruption of the atmospheric boundary layer by jets. In addition, jet-shear flow interaction has important applications in film cooling, impingement cooling, mixing of two fluid streams and boundary-layer control.

An axisymmetric turbulent jet penetrating perpendicularly a plane shear flow is, inherently, a more complex problem than that of a jet entering a quiescent medium or interacting with a uniform velocity stream. A jet normally impinging on a shear flow produces high rates of mixing between the two flows. The resultant exchange of momentum causes the deflection of the jet axis, the distortion of jet shape to a horse-shoe configuration and development of a complex mixing layer around the jet.

Flow patterns of a turbulent wall jet have been investigated to a considerable extent in the recent past. A comprehensive list of background literature on the subject is compiled in Reference 1. The problem of the turbulent wall jet was studied theoretically by Glauert [2]. This study is based on similarity approach. Based on physical

reasoning, it was found that the entire wall-jet flow cannot comply with one overall similarity solution. Consequently, the flow was divided into two regions, i.e., the inner and outer region. The boundary between these two regions is determined by the height of the local maximum velocity where the shear stress is assumed to be zero. A dimensionless velocity profile for the entire flow was obtained, based on a single similarity parameter. This parameter is not constant but depends on the local Reynolds number and varies with the radial distance. However, its variation is very small and, consequently, the resultant velocity field is approximately similar. Measurements presented in References 3, 4, 5 and 6 are in reasonable agreement with Glauert's similarity solution. Recently, it was found that the turbulent shear stress does not vanish at the point of the zero velocity gradient [6]. This result, nonetheless, does not affect the similarity of the velocity profiles.

Experimental investigations of a plane turbulent wall jet interacting with a constant velocity stream are reported in References 7 and 8. Experimental similitude was obtained in both inner and outer layers of the wall jet for mean velocity, turbulent intensity and shear stress distributions. Different characteristic length and velocity scales were employed for these two layers also. In these investigations the wall jet was tangentially injected through a wall slot.

2. OBJECTIVE

The purpose of the present investigation was to study experimentally the flow of a turbulent jet penetrating normally a shear flow. The work sought mainly to obtain similar velocity variation for the resulting interacting flow employing appropriate similarity scales for the various layers of the flow field.

An apparatus capable of providing a controlled wall jet and shear flow had to be constructed. The experimental program was carried out using a long rectangular channel to confine the shear flow. The downward impinging jet was located on the centerline of the channel. The physical situation is depicted in Fig. 2.1. It is important to notice that the shear flow is always unidirectional. Consequently, the interaction differs between the two flows on either side of the jet stagnation streamline. On one side of the streamline the two flows move in opposite directions whereas they are codirectional on the other side.

Paper tufts were used to help visualize the overall qualitative picture of the flow pattern. Detailed surveys of mean velocity using hot-wire anemometers were conducted. Initially, both wall-jet and shear flow were investigated separately in order to ascertain their characteristics. Experimental similitude for the velocity variation of the combined flow was sought for either side of the impinging jet stagnation streamline. This was feasible since the combined-flow velocity profile possessed a point of maximum velocity. Particular characteristic length and velocity scales are set forth to obtain similitude for various flow quantities within the entire flow domain.

3. EXPERIMENTAL APPARATUS

The objective of the experimental program was to investigate the interaction between a turbulent axisymmetric jet and a plane shear flow, with the former being directed perpendicular to the latter. Study of the resulting combined flow features, downstream and upstream of the jet penetration location, was sought. The experimental aim was accomplished simply by injecting a jet perpendicular to a shear flow.

The horizontal shear flow was bound within the walls of a long open channel. This arrangement ensured a shear flow with a mildly favorable pressure gradient and a relatively high local Reynolds number, i.e., $Re_x = O(10^5)$ based on the shear flow free-stream velocity and on the downstream distance. The axis of the vertical jet was aligned perpendicular to the longitudinal axis of the channel, i.e., it coincided with the z-axis. A schematic diagram of the experimental arrangement is displayed in Fig. 3.1 which also shows the system of coordinates and all important dimensions used.

3.1 The Shear Flow Channel

The shear flow channel was made of two parallel plexiglass walls 5/8-in thick. It is 128 in long with a cross-section of 18 x 18 in. The panels were placed on a 3/4-in thick polished aluminum disk which was the diameter of 138 in. As shown in Fig. 3.1, 13 measurement slots were milled in the side wall. These slots are located in the planes $x = 0, \pm 2, \pm 4, \pm 6, \pm 12, \pm 24, +36$ and $+48$ in. The horizontal shear flow was produced by an axial fan (L. J. Wing Mfg. Co. Model A2D2W6) driven by a 1.5 hp DC motor (Peerless Electric Co., Type D-202-K). This fan is capable of generating air speed up to 10 ft/sec. The boundary

layer was artificially thickened by means of roughness installed at the channel entrance (see Fig. 3.1).

3.2 The Jet

The vertical jet was produced by air ejecting from a 2 in diameter, sharp-edged orifice located in a horizontal plane 22.5 in above the flat plate. A 5 hp centrifugal compressor (North American Mfg. Co. Model 20-D2-5), driven by an electrical motor (GE Induction Motor Model 5K225BT675), supplied the air. Jet velocity of up to 400 ft/sec can be obtained at the orifice. Coarse control of the flow was obtained by means of a butterfly valve. An auxiliary exhaust valve was employed for fine adjustment of the jet flow.

3.3 Probe Positioning

The hot-wire probe could be moved continuously along lines parallel to the z-axis by means of an electrically operated traversing mechanism. This mechanism permitted fine control of position within 0.5 mm. Probe positioning in the horizontal plane, i.e., along lines parallel to the x- and y- axes, was performed by means of a manually operated traversing mechanism. The latter permitted control of position within 0.5 mm. A rotation compound permitted angular positioning of the probes with respect to a reference axis within an accuracy of 0.5^{o}. In addition, the vertical alignment of the probe was monitored by means of a telescopic alidade (Kollmorgen Optical Co. Model Mark III). A photograph of the experimental arrangement is provided in Fig. 3.2.

4. EXPERIMENTAL TECHNIQUE AND INSTRUMENTATION

4.1 Velocity and Turbulence Intensity Measurement

The mean velocity was measured by means of a single hot-wire anemometer. The velocity range encountered in this experiment ranged up to a maximum of 75 ft/sec. In this range, the simplified and operational form of the relationship between the heat loss from a wire placed normal to the flow and the undisturbed velocity is given by the so-called King's law

$$E^2 - E_o^2 = A\, U^{\frac{1}{2}} , \qquad (4.1)$$

where E is the actual voltage drop across the wire placed in the flow, E_o designates the voltage drop across the wire in still air (at zero velocity), U denotes the undisturbed air velocity and A is a constant. The latter depends on wire configuration, material, and the properties of air. It may be noted that previously published data on heat transfer from fine heated wires indicate relatively large variations among the results of different experiments [9]. However, in general all of them show a power law dependence on Reynolds number regarding the heat loss. The exponent varies from 0.45 to 0.52, but a square-root law is generally accepted for moderate velocities. A detailed discussion of the variation of the exponent is presented in Reference 10.

If u is the fluctuation parallel to the mean velocity U, normal to the wire, Eq. (4.1) can be written

$$(\overline{E} + e)^2 - E_o^2 = A(\overline{U} + u)^{\frac{1}{2}} , \qquad (4.2)$$

where the overbar denotes time-averaged values, i.e., DC voltage and mean velocity, E_o is a constant under the chosen operating conditions and e is the instantaneous fluctuating voltage corresponding to the fluctuating velocity u. Under the assumption of relatively small fluctuations the higher order terms in the binomial expansion of $(\overline{E} + e)^2$ and $(\overline{U} + u)^{\frac{1}{2}}$ can be neglected. Thereafter, separating the mean and the fluctuating components on both sides of Eq. (4.2), using Eq. (4.1), and taking root-mean-square of both sides, the turbulence intensity defined commonly as $u_{rms}/\overline{U}$ is given by

$$\frac{u_{rms}}{\overline{U}} = \frac{4\,\overline{E}^2}{\overline{E}^2 - E_o^2}\,\frac{e_{rms}}{\overline{E}}\,, \qquad (4.3)$$

where the subscript rms designates square-root of mean square values (time-averaged), i.e., $\overline{(u^2)}^{\frac{1}{2}}$ and $\overline{(e^2)}^{\frac{1}{2}}$.

In obtaining Eq. (4.3) it was assumed that the fluctuating velocity u is small compared to the mean velocity. However, if the ratio $u/\overline{U}$ is, say, 0.4 or more, an error is introduced by neglecting higher order terms in the binomial expansion. For instance, if $u/\overline{U}$ is of order of 0.4, the maximum possible error is of the order of 10%.

Based on the cosine law, the direction of flow was approximately determined by rotating the probe about its own longitudinal axis until a maximum reading was obtained. A three-hole yaw probe (United Sensor, Model W-87) was employed to verify qualitatively the hot-wire reading.

4.2 Hot-Wire Anemometer System

The hot-wire anemometer employed is a novel system designed and built at the Fluid Dynamics and Diffusion Laboratory, Colorado State University. This hot-wire anemometer is a fully transistorized system of constant temperature (CT) type. A description of its characteristics and performance is presented in Reference 11. The frequency response of the system is flat from DC to beyond 100 kHz and its signal-to-noise (S/N) is greater than 500.

The wire resistance can be measured by this unit with a resolution of 0.005 Ω . The bridge current and/or voltage can be read with an accuracy of 0.1 mA and/or 1 mV, respectively, on the digital meter provided with the unit. A variable cut-off low pass filter, which can be varied in steps from 1 to 100 kHz, is incorporated into the system. A built-in DC suppression network can be used to suppress any desired DC voltage. In addition, the unit is equipped with an output amplifier module. The output signal can be amplified in steps up to a gain of 100.

In connection with the hot-wire anemometer unit the following auxiliary equipment was used:

(1) A root-mean-square meter (DISA, Model 55D35) for measurement of rms values;

(2) A dual-beam oscilloscope (Tektronix, Type 502A) for quick assessment of the output signal pattern;

(3) An x-y plotter (Mosely, Model 135 A) for recording the DC output of the anemometer;

(4) A digital DC Voltmeter (Hewlett-Packard, Model 3440A) for monitoring the DC output voltage;

(5) Attenuators for attenuation of the anemometer output signal to suitable levels for various purposes;

(6) An Equibar Pressure Meter (Transonic, Model 120) for measurements of flow velocities in conjunction with the yaw probe and hot-wire calibration.

A block diagram of the anemometer system and the additional equipment is depicted in Fig. 4.1. A general view of the equipment is shown in Fig. 4.2.

A tungsten wire of nominal diameter 0.00035 in and 0.04 in effective length (1/d = 116) was used. A single wire straight probe of 1/8-in diameter was utilized.

4.3 Hot-Wire Calibration

The hot wire was calibrated over the entire operational velocity range, i.e., 2 to 60 fps, at the beginning and at the end of each run. A calibrator (TS Calibrator, Model 1125) was employed for this purpose. Before every run, particular attention was paid to clean the hot wire using a concentrated cleaning solution made of potasium chromate and sulfuric acid ($K_3CrO_4 + H_2SO_4$).

A sample of the kind of calibration curves obtained is provided by Fig. 4.3. Computation of the exponent of $\overline{U}$ (by plotting log $(\overline{E}^2 - E_o^2)$ vs. log $\overline{U}$ and measuring the slope) showed that it differed from 0.5 by about 10% in the high range of velocity, i.e., 8-60 fps. In general, the linear calibration curves obtained were the best-fit curves in the measured velocity range.

A survey of all the calibration curves of the different wires used revealed a scattering in the values of A within 10 to 15%. This can

be attributed to variation of air properties, aging of the wires in the course of operation, and slight changes in wire material properties.

5. EXPERIMENTAL RESULTS

The experimental investigation reported in this work had the following main objectives:

a) To study the flow field of a turbulent wall jet interacting with a horizontal shear flow,

b) To examine the possibility of achieving similar velocity profiles and, hence, to obtain the appropriate similarity parameters for the resulting flow.

The physical situation investigated, and the system of coordinates used are portrayed in Fig. 2.1. In addition, all important parameters related to the combined flow are shown in Fig. 5.1. The origin of the system of coordinates is selected at the geometrical center of the channel which corresponds to the theoretical stagnation point of the jet. The results are presented in dimensionless form unless mentioned otherwise. Dimensional variables, wherever used, are denoted by an asterisk. As the results are presented, pertinent discussions are interspersed wherever deemed helpful for proper interpretation of the experimental results.

All the measurements presented hereinafter were performed at a constant jet efflux velocity $W_o^* = 190$ ft/sec and at a shear flow free-stream velocity U_{os}^* at station $x^* = -24$ in maintained at 5.2 ft/sec.

5.1 Establishment of the Flow

To begin with, the wall jet and the shear flow were investigated independently to obtain their characteristics. The velocity was measured using a single hot-wire anemometer probe. Measurements of velocity were

carried out at 13 stations along the x-axis, i.e., along the flow axis of symmetry in plane $y^* = 0$. The location of these stations is shown in Fig. 3.1. At each station, the measurements were performed in z-direction at a maximum of 17 positions over a distance of 4 in. The exact number of the positions, at each station, was based on the local total boundary-layer thickness. In carrying out these measurements, the hot-wire axis was positioned vertically, i.e., parallel to the z-axis. In addition, the hot wire also was positioned for maximum output voltage. According to the cosine law [12], the hot wire is most sensitive to the resultant normal velocity [13a, 13b]. Consequently, the flow pitch angle, i.e., the angle in the plane $y^* = 0$ with respect to the x-axis, was monitored by appropriate positioning and rotation of the hot wire. A subsequent verification of velocity direction was conducted by means of a three-hole yaw probe. Visualization by means of paper tufts indicated clearly that the flow was symmetrical with respect to the x-axis.

5.1.1 The wall jet

Along the channel centerline, i.e., along the x-axis in plane $y^* = 0$, the wall jet velocity profiles are symmetrical with respect to the jet stagnation streamline (plane $x^* = 0$). Consequently, only results for the positive side $(x^* > 0)$ within the domain of established flow are presented. The latter is defined as the region where similar velocity profiles are obtained [3]. It was found that this region starts at a distance of approximately 6 in from the jet stagnation streamline, i.e., at $x^* = \pm 6$ in. Samples of the measured mean velocity changes with height at four stations, viz., at $x^* = 6$, 12, 24 and 36 in, are

shown in Fig 5.2. The results are presented using the usual wall jet dimensionless formulation, i.e., $U_j = U_j^*/U_{mj}^*$ and $z = z^*/\delta_{2j}^*$, where U_{mj}^* is the local maximum velocity and δ_{2j}^* is the total boundary-layer thickness. Notice that both U_{mj}^* and δ_{2j}^* are functions of x^*. The total boundary-layer thickness is defined, as commonly done, as the height where $U_j = 0.5$ (for a wall jet, by definition, $U_o = 0$). The longitudinal distance is made dimensionless using the jet orifice radius, i.e., $x = x^*/R^*$, where $R^* = 1$ in (see Fig. 3.1). No results beyond $z = 1.4$ ($z^* = 0.76$ to 4 in depending upon the longitudinal position) are shown due to entrainment effects in the outermost part of the flow.

The local wall jet Reynolds number based on local peak velocity U_{mj}^* and jet width δ_{tj}^* ranges from 4400 to 9500 ($\nu = 2 \times 10^{-4} ft^2/sec$). The jet width is $\delta_{tj}^* = \delta_{2j}^* - \delta_{mj}^*$, where δ_{mj}^* is the inner boundary-layer thickness corresponding to the height of maximum velocity U_{mj}^*. According to the wall jet theory [2, 3], the velocity variation depends upon a single similarity parameter α which is related to the jet Reynolds number. Within the aforementioned Reynolds number range, the value of α varies from 1.26 to 1.31. A sample of the theoretical velocity change at an average Reynolds number of 7000 and for $\alpha = 1.28$ is also depicted in Fig. 5.2. A reasonable agreement to the experimental results is observed.

It is, further, important to examine whether the peak velocity and the thickness of the outer boundary layer vary according to simple power laws, i.e., $U_{mj}^* \sim x^{*a}$ and $\delta_{2j}^* \sim x^{*b}$. The similarity exponents a and b depend on the parameter α [2]. The variations of U_{mj}^* and δ_{2j}^* with distance from the origin are displayed in Fig. 5.3. In this

figure, the peak velocity and the total boundary-layer thickness are made dimensionless using the jet efflux velocity and the jet orifice distance from the flat plate, respectively, i.e., $U_{mj} = U^*_{mj}/W^*_o$ and $\delta_{2j} = \delta^*_{2j}/h^*$. The longitudinal distance is referred to the jet orifice radius, i.e., $x = x^*/R^*$. It was found that $a = -1.19$ and $b = 0.95$. For $\alpha = 1.28$, the corresponding theoretical values [2] of a and b are -1.14 and 1.028 respectively. Thus, the changes in peak velocity and total boundary-layer thickness are in agreement with the jet theory. Insofar as the turbulence intensity variation, similar change as reported in References 5 and 6 was observed.

5.1.2 The shear flow

All the measurements were carried out in plane $y^* = 0$, i.e., along the x-axis, at a constant free-stream velocity $U^*_{os} = 5.2$ ft/sec at station $x^* = -24$ in. Due to the channel flow, the velocity at the outer edge of the boundary layer (the free-stream velocity) is expected to vary with downstream distance. Consequently, a turbulent boundary layer with a mildly favorable pressure gradient was anticipated. It was found that the free-stream velocity changed from its value at $x^* = -24$ in to about 12.1 ft/sec at $x^* = 24$ in. The corresponding average variation in the pressure gradient was of the order of -0.008 mm Hg/ft.

The mean velocity variation with height was measured at 5 stations, viz., at $x^* = -12$, 0, 12, 24 and 36 in. The results are shown in Fig. 5.4 using the usual shear flow dimensionless formulation, i.e., $U_s = U^*_s/U^*_{os}$ and $z = z^*/\delta^*_s$, where U^*_s denotes the mean velocity and δ^*_s designates the local boundary-layer thickness. The Reynolds number of the flow based on local free-stream velocity and local boundary-layer

thickness ranged from 6,200 to 16,600. Hence, a turbulent boundary layer was obtained [14].

Generally, the velocity variation within a turbulent boundary layer on a smooth flat plate can be represented by an empirical power law of the form $U_s \sim z^{1/n}$ [15]. The value of n depends on the flow Reynolds number and can vary from 3 to 10 [16]. It was found that the measured velocity distribution changes satisfactorily according to a power law. The value of n was approximated to be 6.7. For the sake of comparison, the measurements presented in References 17 and 18 are also displayed in Fig. 5.4. In both cases, results corresponding to Reynolds number of the order of 10,000 are portrayed. It is important to note that the data used from Reference 18 was obtained under a mildly favorable pressure gradient of the order of -0.0047 mm Hg/ft. The results shown in Fig. 5.4 are in good agreement with the measurements reported in the aforementioned two references. The growth of the boundary-layer thickness along the x-axis is depicted in Fig. 5.5. In this figure, the boundary-layer thickness is made dimensionless using half-width of the channel, i.e., $\delta_s = \delta_s^*/B^*$, where $B^* = 9$ in (see Fig. 4.1). It was found that the boundary-layer thickness increases with the power $x^{0.77}$ of the distance. The turbulence intensity was measured simultaneously with the mean velocity measurement. By and large, the turbulence intensity revealed a variation similar to that presented in Reference 17. No noticeable deviations from the expected change were found. Consequently, the shear flow was deemed adequate for this experiment.

5.1.3 The combined flow

A series of trials were conducted using paper tufts in order to obtain an overall picture of the interacting (or combined) flow

pattern. The effect of the shear flow on the wall jet was clearly observed.

Next, a detailed survey of the combined flow using a three-hole yaw probe was carried out. The magnitude and, particularly, the velocity direction at various stations, were obtained. These stations were all located in the plane of symmetry, i.e., plane $y^* = 0$. Consequently, only the pitch angle was monitored. An overall mapping of the combined flow streamlines is depicted in Fig. 5.6. The streamlines were graphically approximated and velocity interpolation was employed where needed. As a result of the interaction, the jet stagnation point was observed to shift about 2 in downstream of its theoretical position. Moreover, in the vicinity of the z-axis the streamlines exhibit a sharp curvature. This curvature is indicative of the strong velocity gradient and mixing resulting from the interaction of the two flows. The longitudinal extent of this intense mixing region depends on the height above the plate. Close to the wall, this region stretches up to about 6 in on either side of the z-axis.

To test whether the shear flow was able to penetrate throughout the wall jet and to reach the downstream side of its stagnation streamline, the longitudinal kinetic energy over the entire boundary layer of the combined flow, the wall jet, and the shear flow, was computed. The kinetic energy per unit mass and per unit area normal to the velocity over the entire boundary layer is

$$E_i^* = \frac{1}{\delta_i^*} \int_0^{\delta_i^*} U_i^{*2}\, dz^*, \qquad (5.1)$$

where i stands either for the combined flow $(E_c^*, \delta_{2c}^*, U_c^*)$, the jet $(E_j^*, \delta_{2j}^*, U_j^*)$ or the shear flow $(E_s^*, \delta_s^*, U_s^*)$. In each case, the integral was numerically evaluated. The ratios of the jet and shear flow energy to the combined flow energy, respectively, are shown in Fig. 5.7. The energy variation evidenced that the interaction occurred on both sides of the jet stagnation streamline. For instance, on the upstream side, the jet energy is everywhere larger than that of the combined flow, whereas on the downstream side it is smaller. This is due to the interaction mechanism and to the gradually diminishing effect of the shear flow. However, the shear flow was able to penetrate and perturb the wall jet throughout. Hence, the flow was considered adequate for the experiment.

5.2 Mean Velocity Survey

The main objective of the combined flow mean velocity survey was to explore the possibility of obtaining similar velocity distribution within the boundary layer. Basically, the quest for similitude consists of defining and finding appropriate scale factors or similarity parameters. However, it is worth pointing out that experimental similitude parameters are not necessarily identical to analytical similarity functions [7]. Both components of the interacting flow, i.e., the wall jet and the shear flow, exhibit similitudes in their respective velocity variations. Consequently, it is reasonable to expect that the combined flow would also reveal similar velocity profiles.

It is important to note that the flow upstream of the jet stagnation streamline $(x < 0)$ is different from that in the downstream domain $(x > 0)$. The dissimilar features are discerned by the streamline

pattern and energy variation shown in Figs. 5.6 and 5.7, respectively. The different characteristics are due to the interaction mechanism. The jet spreads in both directions whereas the shear flow is unidirectional. Upstream of the jet stagnation streamline the shear flow opposes the jet while downstream of it both flows are codirectional.

As mentioned earlier, all the velocity measurements were performed along the x-axis, i.e., in the flow plane of symmetry. Within the fully developed flow regime, the predominant velocity along the x-axis is the longitudinal component U. The transverse velocity component V vanished due to symmetry. The vertical velocity component W was found to vary roughly up to 15 to 20% of the longitudinal velocity. To a first approximation, the vertical component is neglected. This approximation for $|x^*| > 6$ in is substantiated by the streamline patterns depicted in Fig. 5.6. Therefore, the results presented hereafter concentrate on the axial velocity U within the fully established flow domain, i.e., for $|x^*| > 6$ in.

The combined flow boundary layer can be viewed qualitatively as a wall-jet like boundary layer. Similar to the wall jet, the combined flow boundary layer is divided into an inner and an outer layer, respectively, as portrayed in Fig. 5.1. These layers are delineated using excess velocities or velocity differences to distinguish from a simple wall jet. The excess velocities are defined in terms of the local free-stream velocity U_o^* peculiar to the interacting flow. Then, the local excess velocity is

$$\Delta U^* = U^* - U_o^* . \qquad (5.2)$$

Similarly, the maximum excess velocity is

$$\Delta U_m^* = U_m^* - U_o^* \quad . \tag{5.3}$$

In these relationships U^* is the local velocity and U_m^* is the local maximum velocity. The thickness of the inner layer δ_m^* corresponds to the height where ΔU_m^* is observed. The total boundary-layer thickness δ_2^* is defined as the maximum height where $\Delta U^* = 0.5\ \Delta U_m^*$, i.e., the height where the local velocity is $U_2^* = 0.5\ (U_m^* + U_o^*)$. Hence, the outer-layer thickness $\delta_t^* = \delta_2^* - \delta_m^*$. In the absence of a shear flow $U_o^* = 0$ and, then, the aforementioned definitions become identical to those for a wall jet.

In presenting the results, the axial distance x^* is made dimensionless throughout by referring it to the jet orifice radius R^*, i.e., $x = x^*/R^*$. Due to different features of velocity variations, the results for the downstream $(x > 0)$ and the upstream $(x < 0)$ domains are presented separately.

5.2.1 Downstream domain

The domain of established flow, as shown in Fig. 5.6, starts at $x^* = 6$ in approximately, i.e., about 4 in from the observed stagnation point. The measured velocity distribution at stations $x^* = 6$, 12, 24, 36 and 48 in employing the usual wall jet parameters, i.e., $U = U^*/U_m^*$ and $z = z^*/\delta_2^*$ is displayed in Fig. 5.8. The velocity profiles do not collapse on a single curve. The inadequacy of wall jet similarity parameters to represent the combined flow is due to the interaction between the shear flow and the wall jet. Basically, in the

case of a wall jet interacting with a shear flow, the inner-layer characteristics depend upon the local maximum velocity U_m^* . On the other hand, it is reasonable to assume that the outer-layer features are determined by the velocities encountered at both extremities of this layer, i.e., by U_m^* and U_2^* . Consequently, the velocity variation within the outer layer depends upon these velocities. These two velocities or the corresponding excess velocities can be considered as the significant velocities of the outer layer. Recall that, for a wall jet U_m^* is the only characteristic velocity. As a result, the use of a single velocity scale for the entire boundary layer is precluded [7, 19].

The velocity variation in the entire boundary layer is affected by both local peak velocity and local maximum excess velocity. Thus, it is interesting to examine their longitudinal variations. Decays of these two velocities in the x- direction are shown in Fig. 5.9, where the velocities are made dimensionless using the jet efflux velocity W_o^* . Within the entire range $x = 6$ to 48 , the maximum velocity U_m decreases smoothly following a power law $x^{-0.47}$. For ΔU_m , however, a decrease following approximately a power law $x^{-0.70}$ is seen only from $x = 12$ to 48 . The deviation observed in the slope of ΔU_m in the region $x = 6$ to 12 is probably due to the local variation of U_o^* .

As mentioned earlier, the thicknesses of the local inner layer, local outer layer and total boundary layer are considered to be characteristic lengths. Hence, it is important to observe their longitudinal variations. Growth of these thicknesses, made dimensionless using the height h^* of the jet orifice above the plate, is depicted in Fig. 5.10. The changes of both inner layer thickness δ_m and total

boundary-layer thickness δ_2 do not obey a simple power law. The inner layer behaves as a plane turbulent boundary layer on a flat plate. Its thickness δ_m increases following a Reynolds number power law $Re_x^{0.84}$, where $Re_x = U_m^* x^*/\nu$, up to $x = 36$ in [15]. The outer-layer thickness δ_t was computed, based on the measurement of δ_2 and δ_m. Undoubtedly, δ_t is a characteristic length for the outer layer. Its eventual use as a similarity length scale is sought. However, within the outer layer, due to the nature of interaction between the jet and the shear flow, the requirements for similarity are expected to be different than those proposed for a simple wall jet. As a result, simple power law variations in x of a characteristic velocity and/or a characteristic length become merely fortuitous.

Variations of the various significant velocities and thicknesses clearly indicate that no single length and/or velocity can be employed as appropriate scaling parameters for the entire boundary layer. Therefore, an analysis for similarity is carried out separately for the inner and outer layer.

A. *Inner Layer.* The inner layer is essentially similar to the inner layer of a wall jet. The velocity variation within the latter can be approximated by that of a turbulent boundary layer on a flat plate [3, 5]. Hence, the velocity and the length similarity parameters are the local maximum velocity U_m^* and the inner-layer thickness δ_m^*. Velocity variations in the vertical direction, are displayed in Fig. 5.11, where the velocity and height were made dimensionless employing the above scales. All the profiles do collapse on a single curve. The minor scatter close to the wall $(z < 0.3)$ is attributed to uncertainty

errors in measurements. *An overall similitude is attained in the inner layer.*

B. *Outer layer.* The velocity decrease with height in the outer layer, (see Fig. 5.8) indicates that U_m^* significantly influences the velocity variations within its lower region. On the other hand, the gradual velocity decrease close to the upper edge of this layer is dominated by U_2^*. Since U_2^* is defined in terms of both U_m^* and U_o^* by Eqs. (5.2) and (5.3), the free-stream velocity U_o^* affects the velocity change in the upper part of the outer layer. This type of velocity variation suggests the division of the outer layer into two zones to reflect the effects of the corresponding dominant velocities U_m^* and U_2^* (or U_o^*). Based on the observed velocity variations, the outer layer is divided into two zones of equal thickness which are depicted in Fig. 5.1. The lower half, or Zone I, extends from the edge of local inner layer to a height $\delta_1^* = 0.5(\delta_m^* + \delta_2^*)$. The upper half, or Zone II, has a thickness of $\delta_2^* - \delta_1^* = 0.5\delta_t^*$.

To obtain similar velocity profiles, appropriate velocity and length scales are formulated for each zone. It appears reasonable to select the velocity and length scales in terms of the characteristic excess velocities and zonal thicknesses. Within Zone I, the maximum excess velocity ΔU_m^* and the thickness of the zone $\delta_1 - \delta_m$ are selected as the characteristic velocity and length, respectively. In Zone II, the local excess velocity

$$\Delta U_j^* = U_1^* - U_o^* , \tag{5.4}$$

is chosen as the velocity scale, and the zonal thickness

$$\delta_2^* - \delta_1^* = 0.5\delta_t^* , \tag{5.5}$$

is used as the length scale.

The velocity profiles in Zone I using the aforestated scales are depicted in Fig. 5.12, where the dimensionless excess velocity and excess height are

$$\psi_1 = (U^* - U_o^*)/(U_m^* - U_o^*) \tag{5.6}$$

and

$$\zeta_1 = (z^* - \delta_m^*)/(\delta_1^* - \delta_m^*) . \tag{5.7}$$

Velocity variations, at all stations, collapse on a single similar profile. An interesting feature of this profile is that the dimensionless excess velocity does not decrease beyond 10% from its maximum value.

The velocity profiles in Zone II rendered dimensionless by aforementioned velocity and length scales are presented in Fig. 5.13. It may be noted that, the local velocity U_1^* corresponding to the height δ_1^* is 5 to 10% higher than the arithmetic mean of U_m^* and U_2^*. The dimensionless excess velocity and excess height are defined as

$$\psi_2 = (U^* - U_o^*)/(U^*_1 - U_o^*) \tag{5.8}$$

and

$$\zeta_2 = (z^* - \delta_1^*)/(\delta_2^* - \delta_1^*) \ . \qquad (5.9)$$

The velocity variations at all stations are represented by a single curve. Hence, *a similarity velocity profile is obtained for Zone II.* The excess velocity ψ_2 is seen to decrease rather sharply. It attenuates to about 60% of its maximum value at the outer edge.

5.2.2 Upstream domain

On the upstream side of jet stagnation streamline, the domain of established flow was found (see Fig. 5.6) to develop from $x^* = -6$ in approximately, i.e., 8 in from the observed stagnation point. Measured velocity variation with height at $x^* = -6$, -12 and -24 in is portrayed in Fig. 5.14. The velocity and height are made dimensionless as for the downstream domain, employing the wall jet parameters, i.e., $U = U^*/U_m^*$ and $z = z^*/\delta_2^*$. It is evident from this figure and from Fig. 5.6, that at stations $x^* = -12$ and -24 in , a change in the direction of flow occurs during a vertical traverse. At these postions, the zero-velocity points are reached at heights corresponding to or slightly beyond the outer-layer thickness. This flow reversal at stations farther away from the jet stagnation point is attributed to the stronger shear flow opposing the jet. Closer to the jet impingement point, i.e., at $x^* = -6$ in , no flow reversal occurred. For convenience, in presenting the results involving the velocity directed in the negative direction of x-axis, its negative sign is omitted since absolute values are considered. As a result, the reversed velocity is assumed to be negative.

By and large, the velocity variations shown in Fig. 5.14 indicate that in the boundary layer ($z^* \leq \delta_2^*$) the velocity changes are affected by the maximum velocity and the velocity at its edge, i.e., by U_m^* and U_2^*. Similar to the downstream domain, these two velocities can be regarded as the significant velocities of the boundary layer. Moreover, the effect of the counterflow free-stream velocity U_o^* is discerned. Consequently, similar to the downstream domain, excess velocities in terms of U_o^* are used. At $x^* = -12$ and -24 in , the effects of opposing free-stream velocity U_o^* are reflected by steep velocity gradients. Where the counterflow is less predominant, e.g., at $x^* = -6$ in , the velocity profile has a milder slope. Furthermore, at $x^* = -12$ and -24 in , the outer-layer thickness δ_t^* is smaller than the corresponding inner layer thickness δ_m^*. Finally, it is noted that the dimensionless profiles do not merge onto a single curve. Thus no similarity is obtained employing the wall jet parameters, as anticipated from the results on the downstream side.

To gain an insight into the nature of the flow, the various significant velocities and thicknesses, i.e., maximum velocity, maximum excess velocity, inner-layer thickness, outer-layer thickness and total boundary-layer thickness are examined for their longitudinal variations in Figs. 5.15 and 5.16, respectively. The velocity and thicknesses are rendered dimensionless using the same parameters as in the downstream domain. Simple power law variations of these quantities with distance x are improbable, due to the flow interaction. Both velocities, instead of continuously decreasing, tend to level off with increasing distance from the stagnation streamline. This is attributed to the opposing shear flow, which causes an adverse pressure gradient and a concomitant

retardation in the streamwise spreading of the wall jet. In correspondence with the variation of U_m, the inner-layer thickness δ_m exhibits an increase followed by a leveling off. This is clearly observed in Fig. 5.16. The continuous decay of the outer-layer thickness δ_t signifies the trend toward ultimate disruption of the outer layer by the counterflow. Total boundary layer thickness δ_2 increases very slightly with x, following a power law $x^{0.1}$. This increase occurs in spite of a concomitant decrease in δ_t. Thus, stronger interaction occurred on the upstream side, in contrast to the downstream domain where the interaction was weaker. However, the general variation of the significant velocities suggests a flow pattern essentially similar to the downstream side. Consequently, the same scales as in the downstream side are adopted to obtain similar velocity variation.

A. *Inner layer.* In the same manner as for the flow in the downstream side, the local maximum velocity U_m^* and the local thickness of the inner layer δ_m^* are used as the characteristic scales. Variation of velocity with height, where both are made dimensionless utilizing the foregoing scales, is depicted in Fig. 5.17. As expected, the velocity profiles at all stations merge reasonably into a single curve. Clearly, *a similitude variation is obtained.*

B. *Outer layer.* The overall qualitative resemblance between upstream and downstream flow suggests an identical division of the outer layer into two equal zones, i.e., Zone I (lower half) and Zone II (upper half). Furthermore, the same characteristic scales as for the downstream side are used for these two zones. Thus, within Zone I, $U_m^* - U_o^*$ and $\delta_1^* - \delta_m^*$ are employed whereas in Zone II $U_1^* - U_o^*$ and $\delta_2^* - \delta_1^*$ are utilized. Dimensionless velocity profiles for these two zones are portrayed in

Figs. 5.18 and 5.19, respectively. *Similarity velocity variation is clearly observed.* Since similarity was obtained employing the same scales for both upstream and downstream flow, the overall congruence between these two regions is evidenced. The excess velocity ψ_1 in Zone I does not decrease by more than 5% from its maximum value. Within Zone II, the excess velocity decreases to about 40% of its maximum value. The greater attenuation of ψ_2 with height ζ_2, as compared to downstream flow, indicates a stronger interaction between the wall jet and the shear flow. It is interesting to remark that at station $x = -24$, both U_m and U_o possess the same absolute value. Thus, the important aspects of the results are that *similar velocity profiles, for both downstream and upstream domains, were obtained by postulating appropriate velocity and length scales* based on the local characteristic velocity (or excess velocity) and local layer (or zonal) thickness.

5.3 Integral Parameters

In the case of a plane turbulent boundary layer, similarity of velocity profiles is reflected by approximately constant value of the shape factor along the flow direction. Similitude was obtained in the velocity variations for the various regions of the combined flow. Hence, it is interesting to examine the longitudinal variations of the shape factor within each particular layer. Reversal of slope in a velocity profile can cause a singularity in the value of the shape factor if the usual boundary layer conventions are used. To avoid this pitfall, appropriate reference velocities need to be chosen for each distinct region of the flow. In the inner layer, the reference velocity is the

local maximum velocity. For each zone of the outer layer the respective characteristic excess velocity, i.e., ΔU_m or ΔU_1, is selected as the reference velocity. It is hypothesized that the flow in each zone of the outer layer is caused by a sudden displacement of a fictitious plate located at the lower edge of the particular zone. This imaginary plate moves with a velocity $U_m^*(x)$ or $U_1^*(x)$ depending on the zone involved.

The displacement thickness Δ_m^* and momentum thickness θ_m^* for the inner layer are defined as

$$\Delta_m^* = \int_o^{\delta_m^*} \left(1 - \frac{U^*}{U_m^*}\right) dz^* , \tag{5.10}$$

and

$$\theta_m^* = \int_o^{\delta_m^*} \left(1 - \frac{U^*}{U_m^*}\right) \left(\frac{U^*}{U_m^*}\right) dz^* . \tag{5.11}$$

On the other hand, the displacement thickness Δ_i^* and momentum thickness θ_i^* for the two zones of the outer layer are defined in terms of the excess velocities for the two zones. Thus,

$$\Delta_i^* = \int_{\delta_\ell^*}^{\delta_i^*} \left(1 - \frac{U^* - U_o^*}{U_\ell^* - U_o^*}\right) dz^* . \tag{5.12}$$

and

$$\theta_i^* = \int_{\delta_\ell^*}^{\delta_i^*} \left(1 - \frac{U^* - U_o^*}{U_\ell^* - U_o^*}\right) \left(\frac{U^* - U_o^*}{U_\ell^* - U_o^*}\right) dz^* \tag{5.13}$$

where $i = 1,2$ and $\ell = m,1$. Consequently, the zonal shape factor is

$$H_k = \frac{\Delta_k^*}{\theta_k^*} \tag{5.14}$$

where $k = m,1,2$ depending on the particular region.

Calculated values of the shape factor at all stations along the x-axis are shown in Fig. 5.20. On both sides of the stagnation streamline the shape factors in all three regions, i.e., H_m , H_1 and H_2, are found to attain constant values within less than 10% scattering. The values of H_m , H_1 and H_2 are 1.85, 1.03 and 1.55, respectively. The value of the shape factor for inner layer H_m is within reasonable agreement with measured values of the shape factor for a plane turbulent boundary layer with a mild pressure gradient [18]. In this reference, values of shape factor ranging from 1.44 to 1.66 are reported. In general, the obtained values of the zonal shape factor are considered to be characteristic parameters for the three regions of the interacting flow.

5.4 Mean Energy

The mean kinetic energy in a particular stratum of the flow can be considered as being suggestive of the strength of interaction between the wall jet and the shear flow. Consequently, it is interesting to observe the variation of mean kinetic energy in both flow domains, i.e., upstream and downstream of the jet stagnation streamline. Since similar velocity variation was obtained using adequate scales for each region, similitude of the mean kinetic energy change is expected.

In an analogous manner to the velocity, the dimensionless kinetic energy for the inner layer is

$$E = U^{*2}/U_m^{*2}, \tag{5.15}$$

where U^* and U_m^* are the local and the local maximum velocity, respectively. Within the outer layer, the dimensionless local excess energy in Zones I and II are

$$\Delta E_1 = (U^{*2} - U_o^{*2})/(U_m^{*2} - U_o^{*2}) , \tag{5.16}$$

and

$$\Delta E_2 = (U^{*2} - U_o^{*2})/(U_1^{*2} - U_o^{*2}) . \tag{5.17}$$

The dimensionless vertical coordinate utilized for each region is identical to the one used in portraying the velocity similitude (see Sec. 5.2.1).

Both upstream and downstream energy variations in the inner layer are presented in Fig. 5.21. *Similar profiles of energy are clearly observed for either case.* The energy change for the inner layer of the undisturbed wall jet using analogous reference energy and length scales, viz., $1/2\ \rho\ U_{mj}^{*2}$ and δ_{mj}^*, is also shown in the figure. As expected, the local energy of the combined flow is larger than that of the wall jet in the downstream domain. On the other hand, in the upstream domain, where the shear flow opposes the wall jet, the local energy is smaller than that of the wall jet. Thus, the interaction between the wall jet and the shear flow occurred on either side of the jet stagnation streamline.

Profiles of energy distribution for both zones of the outer layer are shown in Fig. 5.22. In each zone, *similarity variation of energy is observed by the approximate collapse of the results on two distinct upstream and downstream curves*. Since it is interesting to compare the energy in the outer layer to that of the unperturbed wall jet, the energy of the latter is also depicted in Fig. 5.22. For the sake of comparison, the outer layer of the unperturbed wall jet was divided into two zones using the same definitions as for the combined flow. The jet energy in the two zones is made dimensionless using $1/2\ \rho\ U^{*2}_{ij}$, where $i = 1,2$ respectively. Recall that for a wall jet U^*_o is zero by definition. Dimensionless excess heights employed for these two zones are identical to those used for the combined flow. The local energy of the combined flow for both upstream and downstream domains is seen to be larger than that of wall jet except for a small region close to the lower edge of Zone II. Recall that for the inner layer a different behavior was obtained. The fact that the local wall-jet energy is smaller than that of the combined flow in both domains stems from the respective energy scales employed. In both zones of the outer layer the energy in the downstream domain attenuates more rapidly than for the upstream side. In Zone I, the rates of decrease of energy do not differ significantly in either flow domain. This indicates that the interactions within this zone on both sides are roughly of the same strength. On the other hand, in Zone II, the energy decrease on the downstream side is much larger than that in the upstream domain. For example, the local energy for the downstream side decays to 60% of its maximum value, while a corresponding decrease to only 80% is observed for the upstream flow.

This is attributed to a concomitant decrease in interaction between the wall-jet outer layer and the shear flow in the downstream side.

It is important to note that the energy variation indicates the occurrence of interaction and eventually permits evaluation of its strength. Furthermore, *the local similarity obtained, clearly shows that all mean flow properties exhibit experimental similitude.*

5.5 Turbulence Intensity Survey

Vertical variations of the longitudinal turbulence intensity based on the local mean velocity

$$T_u = u^*_{rms}/\overline{U}^*(z^*), \qquad (5.18)$$

were measured simultaneously with the mean velocity measurements. Turbulence profiles for both downstream and upstream domains are presented in Fig. 5.23 and Fig. 5.24, respectively, where the vertical coordinate is made dimensionless using the local total boundary-layer thickness δ_2^*. The variations of turbulence intensity on the downstream side are qualitatively similar to that obtained in the case of a wall jet [6]. On the other hand, in the upstream domain, the turbulent intensity changes resemble, by and large, channel flow turbulence variations [17].

Similitude in mean velocities was obtained in each region using the corresponding characteristic velocity or characteristic excess velocity. Consequently, it is important to observe the behavior of turbulence intensity on either side of the jet stagnation streamline, when the rms value of the fluctuating velocity is made dimensionless with respect to the characteristic velocity of each region. Thus, within the inner layer

the turbulence intensity is defined as

$$T_{um} = u^*_{rms}/\bar{U}^*_m \ . \qquad (5.19)$$

In the outer layer, the turbulence intensity in Zones I and II are

$$T_{u1} = u^*_{rms}/(\bar{U}^*_m - \bar{U}^*_o) \ , \qquad (5.20)$$

and

$$T_{u2} = u^*_{rms}/(\bar{U}^*_1 - \bar{U}^*_o) \ , \qquad (5.21)$$

respectively. Next, in order to obtain a similarity variation of turbulence intensity, the same zonal length scales as for the mean velocity are employed. Basically, similarity variation of the flow properties is ensured from using both zonal characteristic velocity and length. Thus, in the inner layer the height is made dimensionless utilizing its thickness δ^*_m . In the two zones of the outer layer the dimensionless excess heights ζ_1 and ζ_2 based on the zonal thicknesses $\delta^*_1 - \delta^*_m$ and $\delta^*_2 - \delta^*_1$, respectively, are employed.

The turbulence intensity variation in the inner layer is shown in Fig. 5.25. All the upstream and the downstream profiles are approximated by two distinct curves. The higher level of turbulence in the upstream domain is caused by the penetration of the inner layer by the counterflow.

Vertical variations of turbulence intensity in Zones I and II of the outer layer are portrayed in Fig. 5.26 and Fig. 5.27, respectively.

All the results for the downstream flow collapse approximately onto a single curve. For the upstream domain, variations of turbulence intensity at stations x = -12 and -24 are coalescent. No similarity was obtained in the upstream domain at x = -6. This is attributed to the location of this station. Recall that the established flow domain starts at about 8 in from the jet stagnation point. Higher levels of turbulence are always prevalent in the downstream domain. It is important to notice that the mean energy exhibits an opposite behavior (see Figs. 5.21 and 5.22). Thus, the use of *appropriate velocity and length scales led to experimental similitude of turbulence intensity.*

6. SUMMARY AND CONCLUSIONS

The experimental results presented in this work indicate that the variation of the mean quantities of the flow resulting from the interaction of a spreading turbulent wall jet on a smooth surface and a shear flow exhibit similarity. The combined flow was formed by a downward-directed circular jet injected normally to a moving shear stream. As a result of the interaction, it was found that the impinging jet stagnation streamline is deflected in the direction of the shear flow. The interaction was observed to occur on both sides of the axis of the impinging jet. Its overall strength differed, depending upon the relative directions of the two interacting flows. In the upstream domain, viz., the domain where the wall-jet velocity opposes the shear flow, stronger mixing was observed and flow reversal occurred. The reversal was monitored at heights beyond the thickness of the boundary layer of the combined flow. In the downstream domain, viz., the domain where both wall-jet velocity and shear flow were coaxial, the occurrence of the interaction was inferred from the energy change.

Similar variation of mean velocity was found to prevail within both flow domains provided that the boundary layer is divided into three characteristic regions and adequate similarity scales are employed. Since the velocity profiles possessed a maximum velocity, the flow was divided into an inner and an outer layer. These layers were delineated, based on the local maximum excess velocity, to distinguish from a simple wall-jet flow. The excess velocity was defined in terms of the local free-stream velocity peculiar to this flow. The outer layer, due to the nature of the velocity change, was subdivided into two zones of equal thickness, viz., Zone I or lower half and Zone II or upper half. Within

each region, velocity and length scales were formulated. In the inner layer the local maximum velocity was used as the similarity velocity scale. For the two zones of the outer layer the local maximum excess velocities were defined as the velocity scales. The thicknesses of the three regions were employed as the length scales. A similar mean velocity variation within each region was obtained despite the fact that neither the velocity scales nor the length scales exhibited a definite change with the longitudinal distance. On the other hand, computation of the shape factor based on the characteristic velocity scales resulted in constant values for it. This result substantiated the similarity in mean velocity change. Moreover, these regional shape factors can be considered as being characteristic to this flow.

The use of analogous scales led to similar variation of the mean energy within the three regions of the flow. Basically, the energy change can be used as an indication of the strength of the interaction. In the inner layer the energy in the downstream domain was everywhere larger than that of a wall jet. On the other hand, in the upstream domain the energy was smaller than that of a wall jet. Within the two zones of the outer layer the energy in both domains was greater than that of a wall jet. Thus, the interaction was stronger in the outer layer.

Similar turbulence intensity profiles were obtained within each region of the flow when the rms value of the turbulent fluctuation velocity was made dimensionless employing the respective similarity velocity scales. In the inner layer the turbulence intensity was higher in the upstream domain due to the opposing shear flow. Within the two zones of the outer layer the turbulence intensity was larger in the

downstream domain indicating the high level of turbulence of this flow.

In conclusion, the division of the flow into three characteristic regions, and formulation of velocity and length scales based on the nature of velocity variation, yielded similar variation of both mean velocity and turbulence intensity.

REFERENCES

1. Rajaratnam, N. and Subramanya, K., "An annotated bibliography on wall jets," U. of Alberta Publications, Edmonton, Canada (1967).

2. Glauert, M. B., "The wall jet," J. Fluid Mech., 1, 3, 625-643 (1956).

3. Bakke, P., "An experimental investigation of a wall jet," J. Fluid Mech., 2, 2, 467-472 (1957).

4. Bradshaw, P. and Love, E. M., "The normal impingement of a circular air jet on a flat surface," NPL RM 3205 (1959).

5. Schwarz, W. H. and Cosart, W. P., "The two-dimensional turbulent wall jet," J. Fluid Mech., 10, 2, 481-495 (1961).

6. Poreh, M., Tsuei, Y. G., and Cermak, J. E., "Investigations of a turbulent radial wall jet," ASME Transactions, J. Applied Mech. 34, 2, 457-463 (1967).

7. Kruka, V. and Eskinazi, S., "The wall jet in a moving stream," J. Fluid Mech., 20, 2, 555-579 (1964).

8. Kacker, S. C. and Whitelaw, J. H., "Some properties of the two-dimensional turbulent wall jet in a moving stream," ASME Transactions, J. Applied Mech., 35, 4, 641-651 (1968).

9. Sadeh, W. Z., Maeder, P. F. and Sutera, S. P., "A hot-wire method for low velocity with large fluctuations," Review of Scientific Instruments, 41, 9, 1295-1298 (1970).

10. Collis, D. C. and Williams, M. J. "Two-dimensional convection from heated wires at low Reynolds numbers," J. Fluid Mech., 6, 3, 357-384 (1959).

11. Sadeh, W. Z., and Finn, C., "A novel hot-wire anemometer system," to be published.

12. Ladenburg, R. W., et al., (editors), Physical Measurements in Gas Dynamics and Combustion, Article F., 2, Kovasznay, L. S. G., "Hot-wire method," 219-285 (High-speed Aerodynamics and Jet Propulsion, Vol. IX, Princeton Univ. Press, Princeton, N.J. 1954).

13a. Champagne, F. M., Sleicher, C. A. and Wehrmann, O. H., "Turbulence measurements with inclined hot wires," Part I, J. Fluid Mech., 28, 1, 153-175 (1967).

13b. Champagne, F. M. and Sleicher, C. A., "Turbulence measurements with inclined hot wires," Part II, J. Fluid Mech., 28, 1, 177-182 (1967).

14. Hinze, J. O., Turbulence (McGraw-Hill, New York, N.Y. 1959).

15. Schlichting, H., Boundary Layer Theory (McGraw-Hill, New York, N.Y. 1968) 6th ed.

16. Clauser, F. H., "The turbulent boundary layer," Advances in Applied Mechanics, Eds. Dryden, H. L., Kármán, von T. et al., Vol. IV, 1-51 (John Wiley, 1956).

17. Laufer, J., "Investigations of turbulent flow in a two-dimensional channel," NACA TR 1053 (1951).

18. Kline, S. J., Reynolds, W. C., Schraub, F. A. and Runstadler, P. W., "The structure of turbulent boundary layers," J. Fluid Mech., 30, 4, 741-773 (1967).

19. Naudascher, E., "On a general similarity analysis for turbulent jets," Iowa Inst. of Hydr. Res., Rep. No. 106, Iowa City, Iowa (1967).

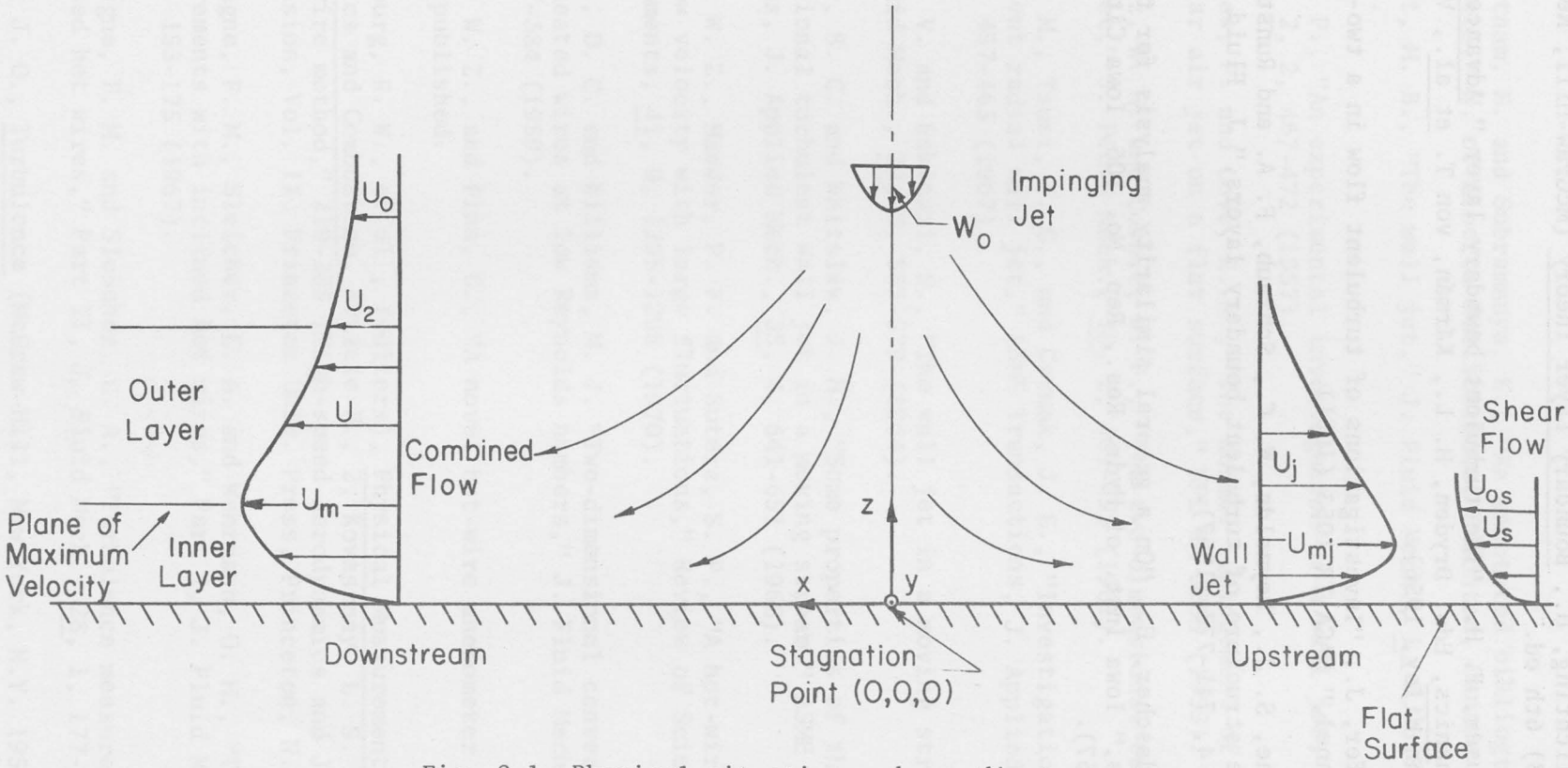

Fig. 2.1 Physical situation and coordinate system.

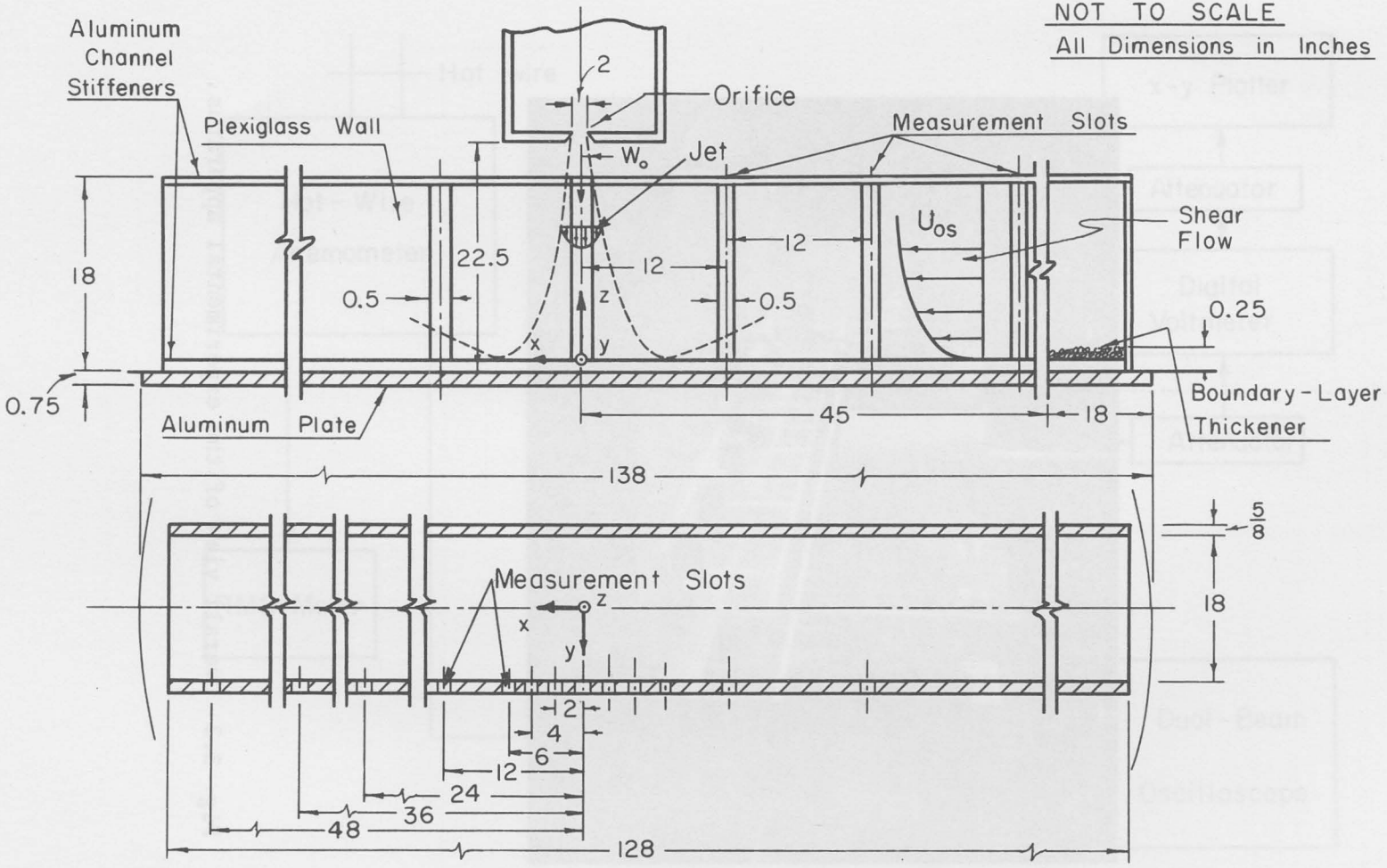

Fig. 3.1 Sketch of the experimental arrangement.

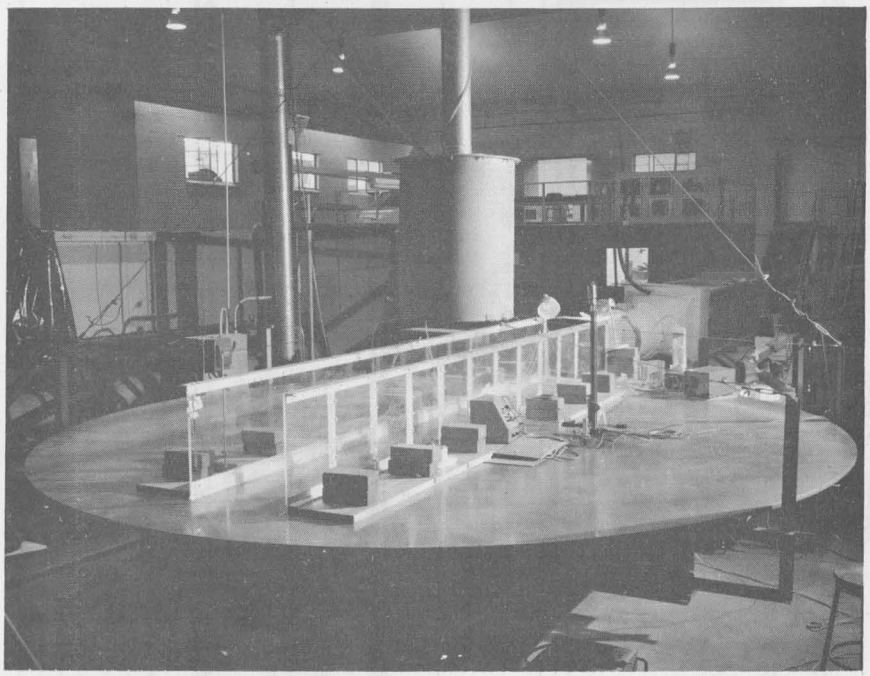

Fig. 3.2 Overall view of the experimental apparatus.

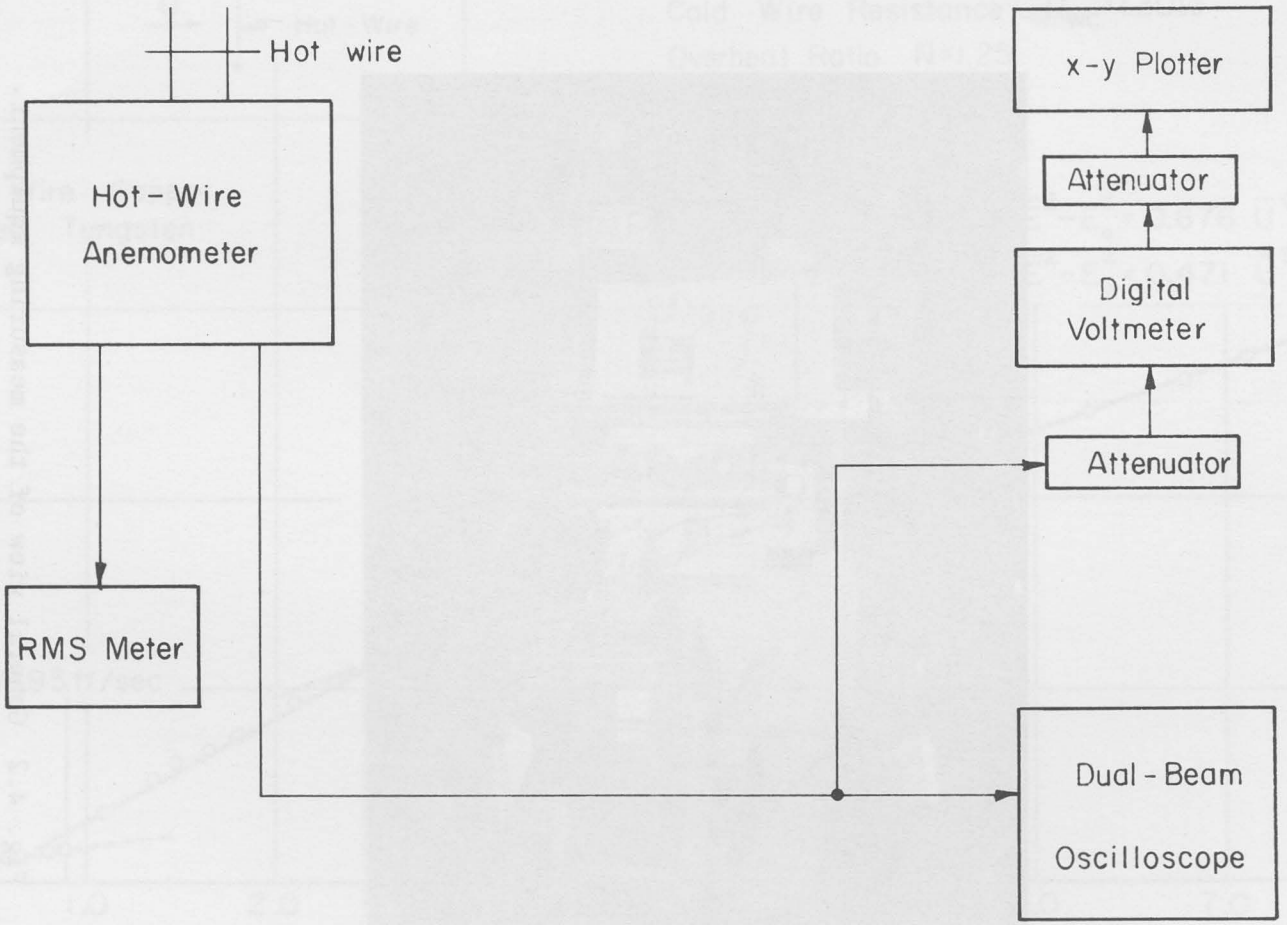

Fig. 4.1 Block diagram of the hot-wire anemometer measuring system.

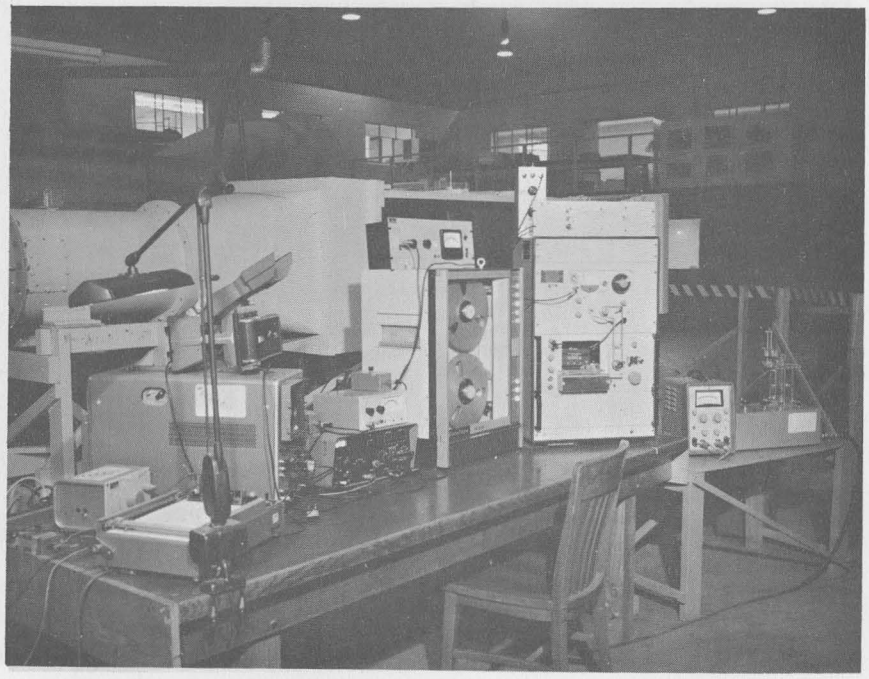

Fig. 4.2 General view of the measuring equipment.

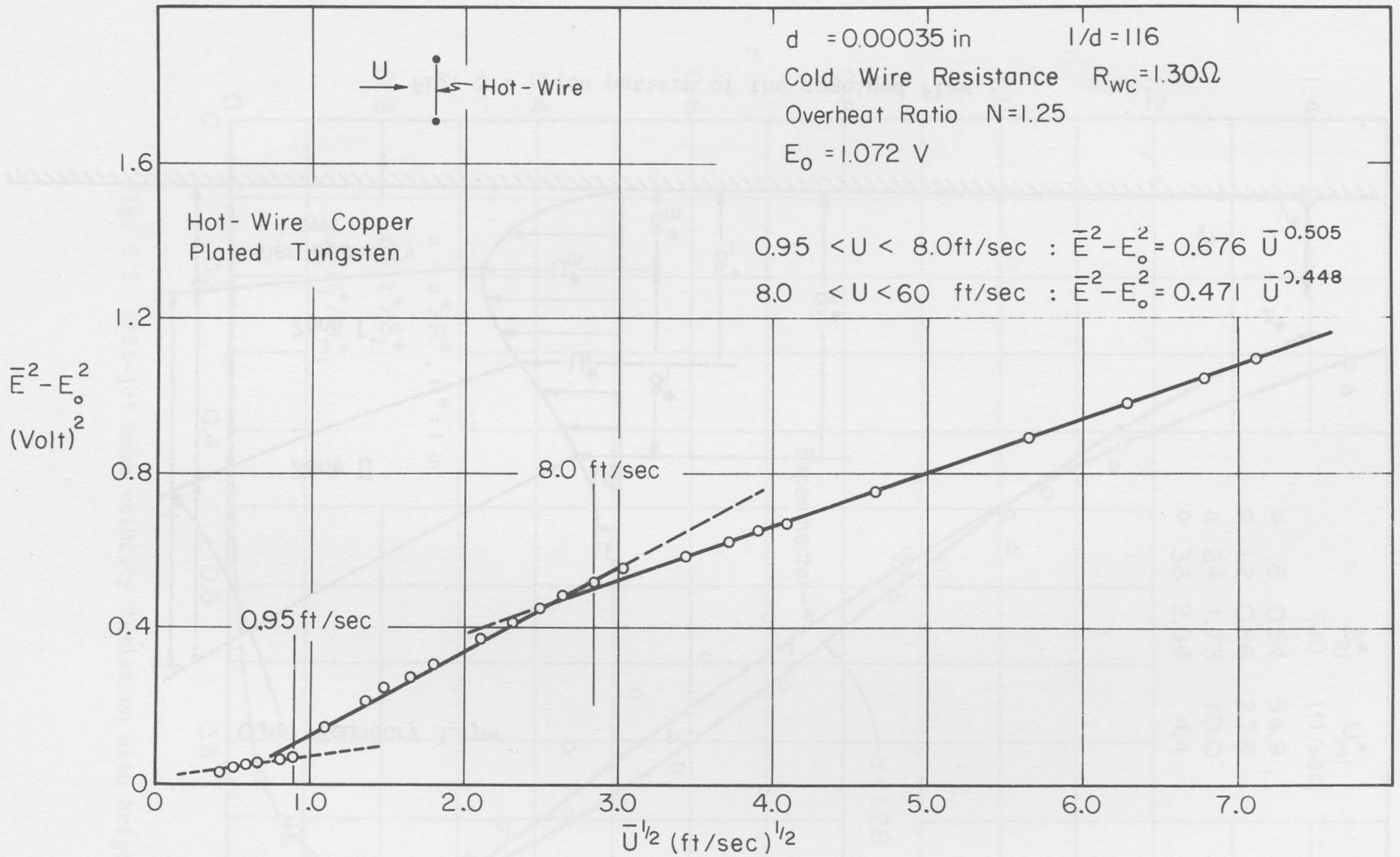

Fig. 4.3 Typical hot-wire calibration curve.

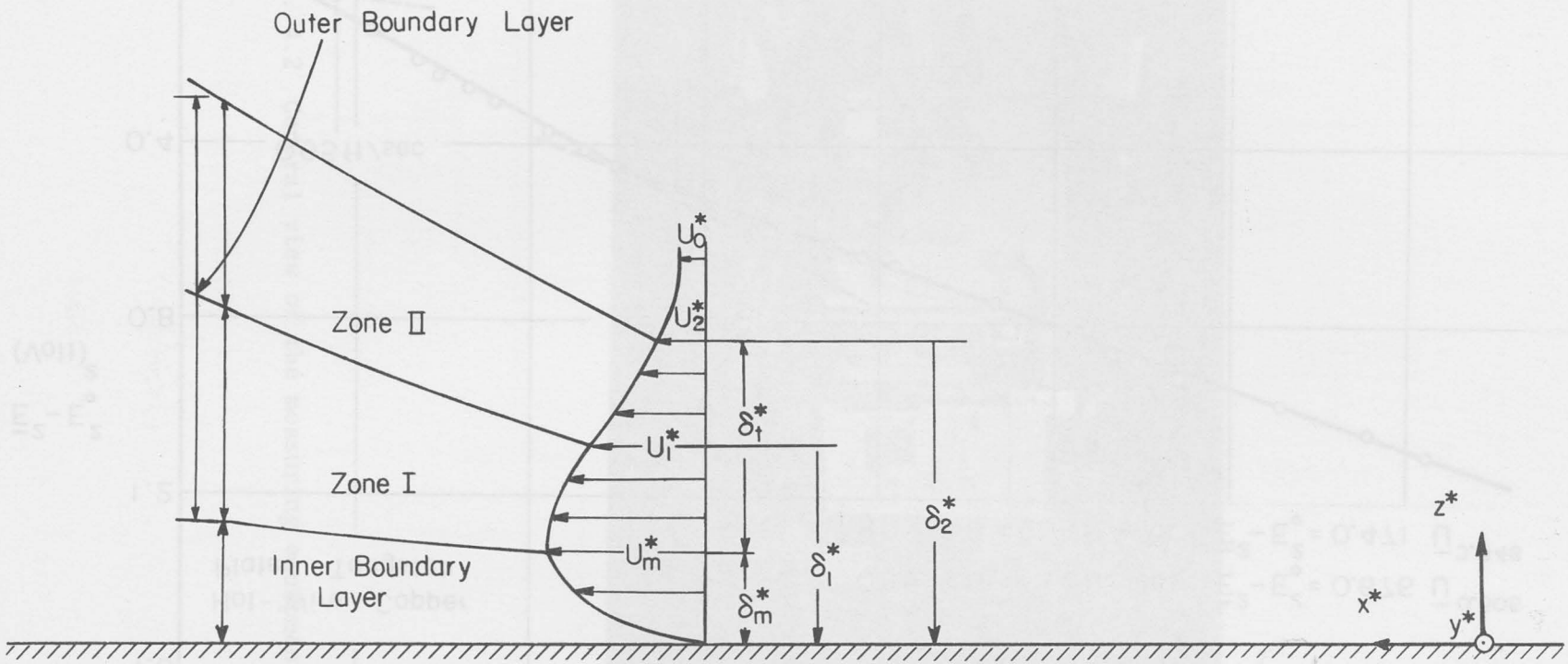

Fig. 5.1 Flow pattern of the combined flow.

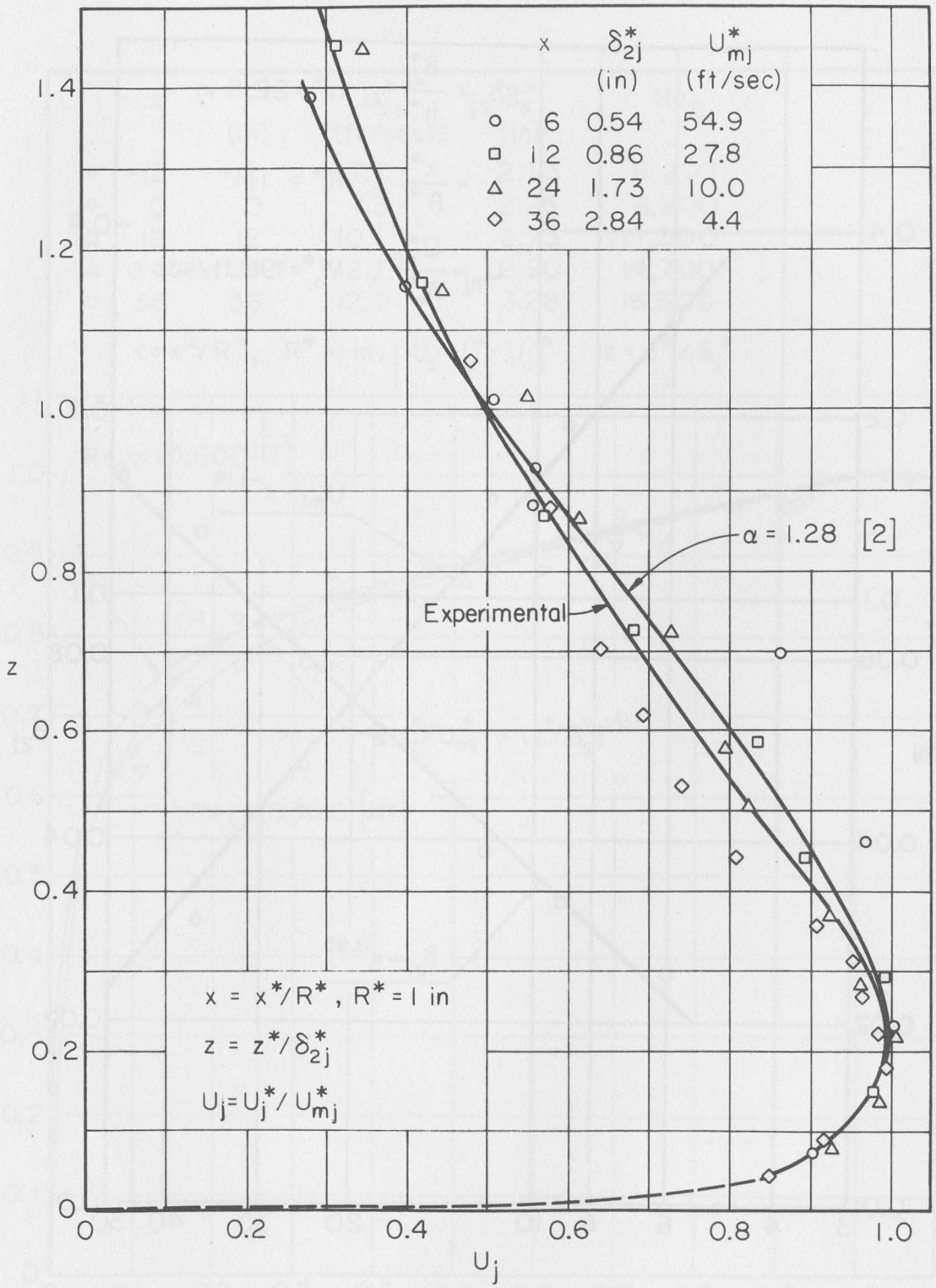

Fig. 5.2 Wall-jet mean velocity variation with height.

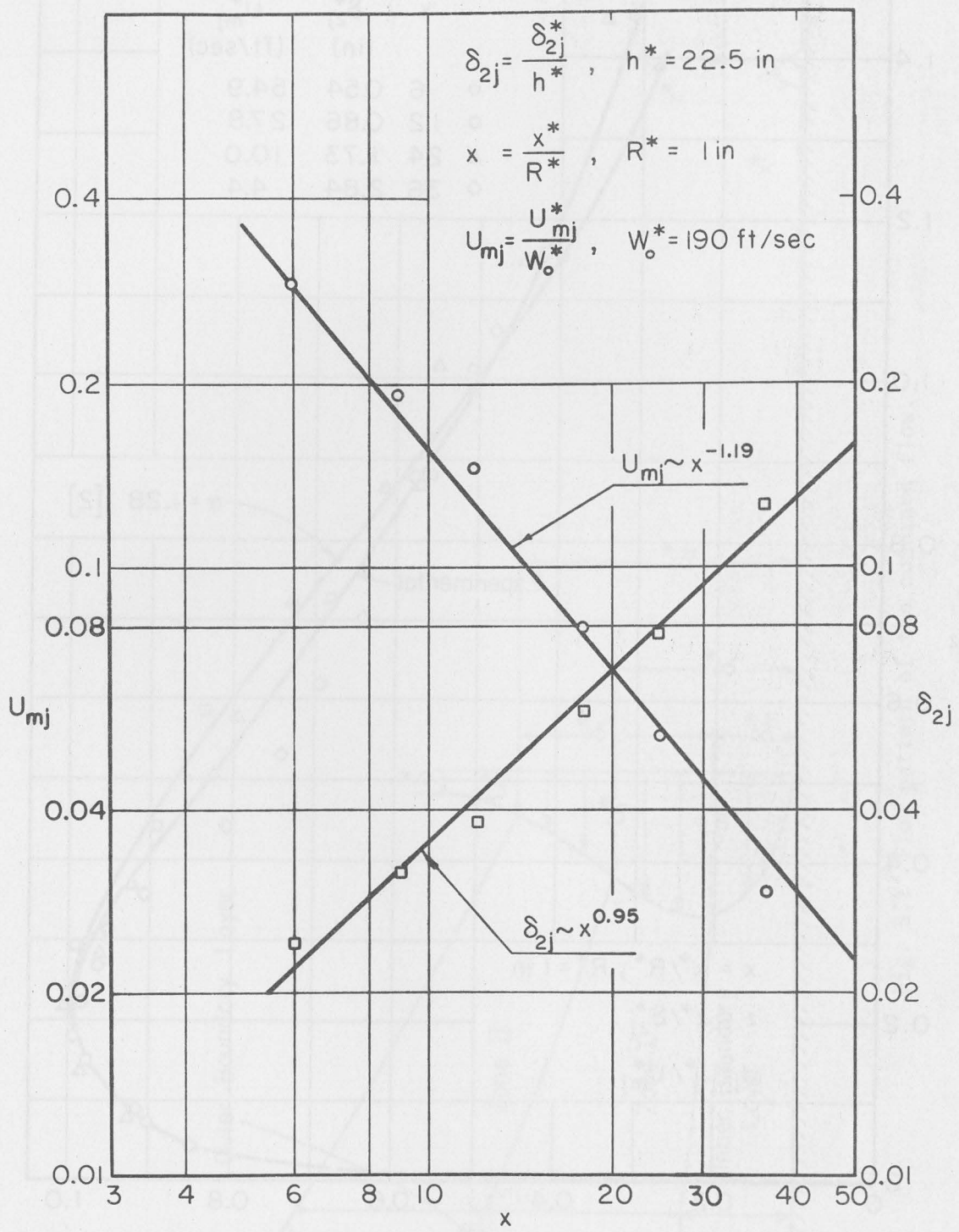

Fig. 5.3 Wall-jet peak velocity decay and total boundary-layer growth .

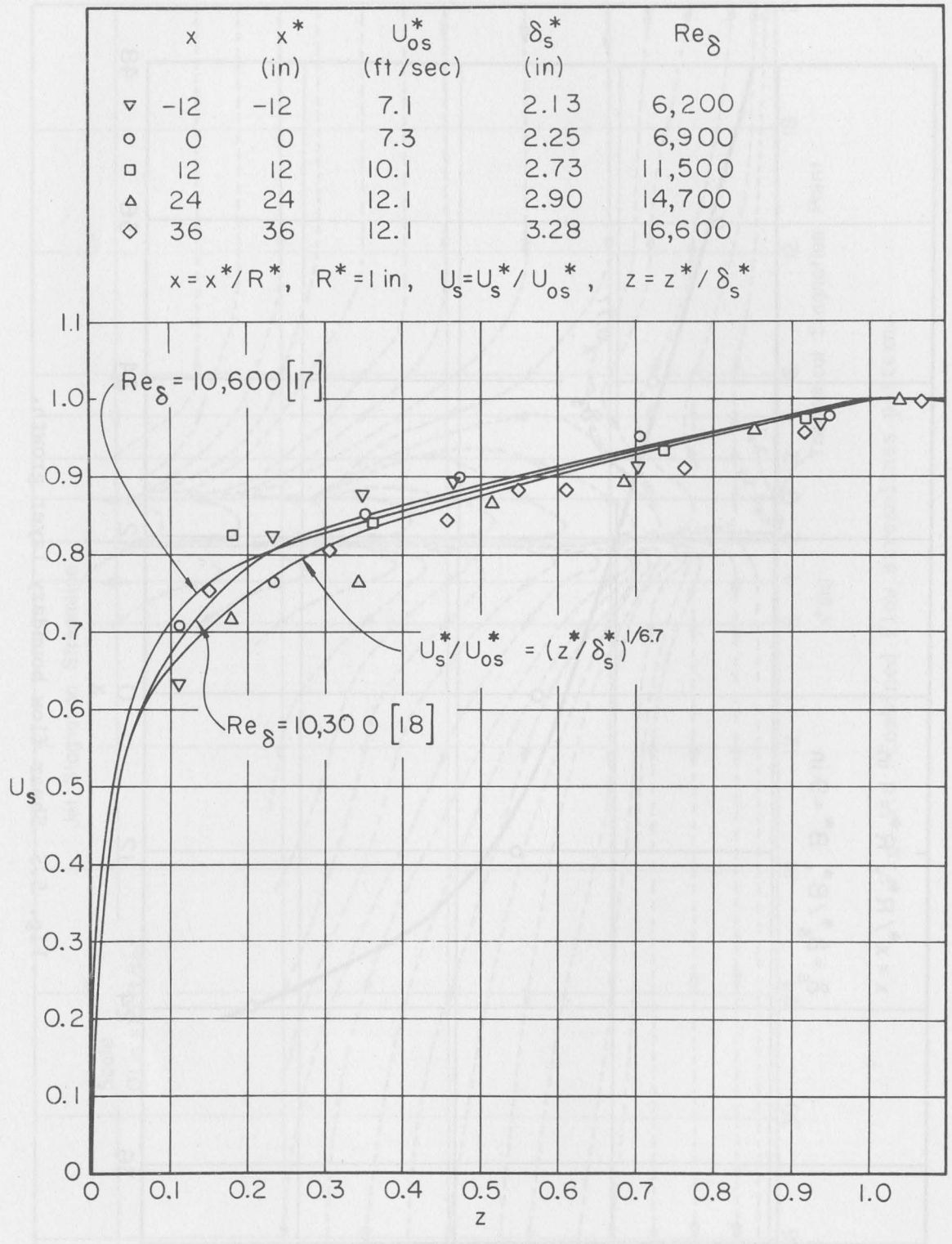

Fig. 5.4 Shear flow mean velocity variation.

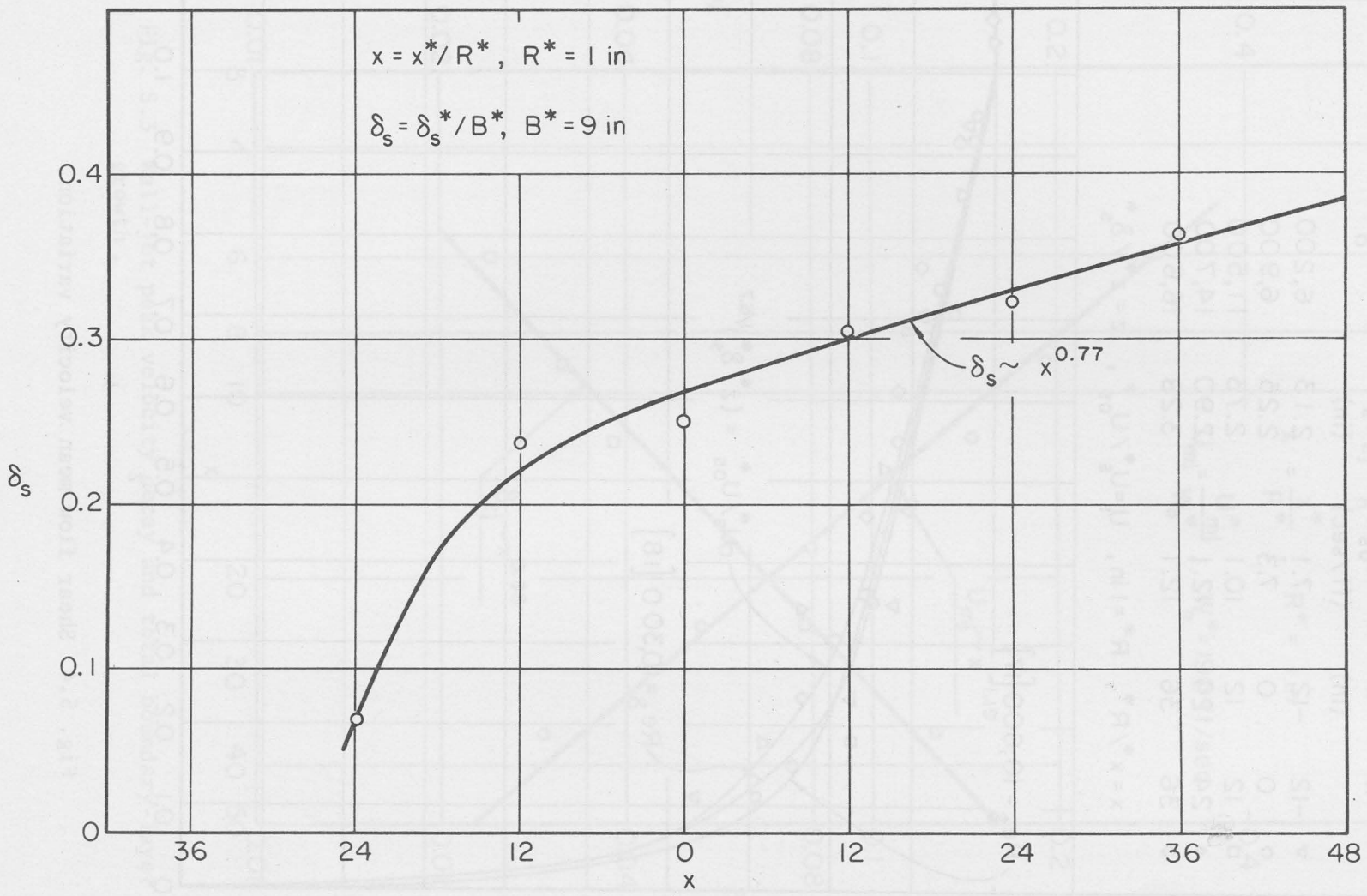

Fig. 5.5 Shear flow boundary layer growth.

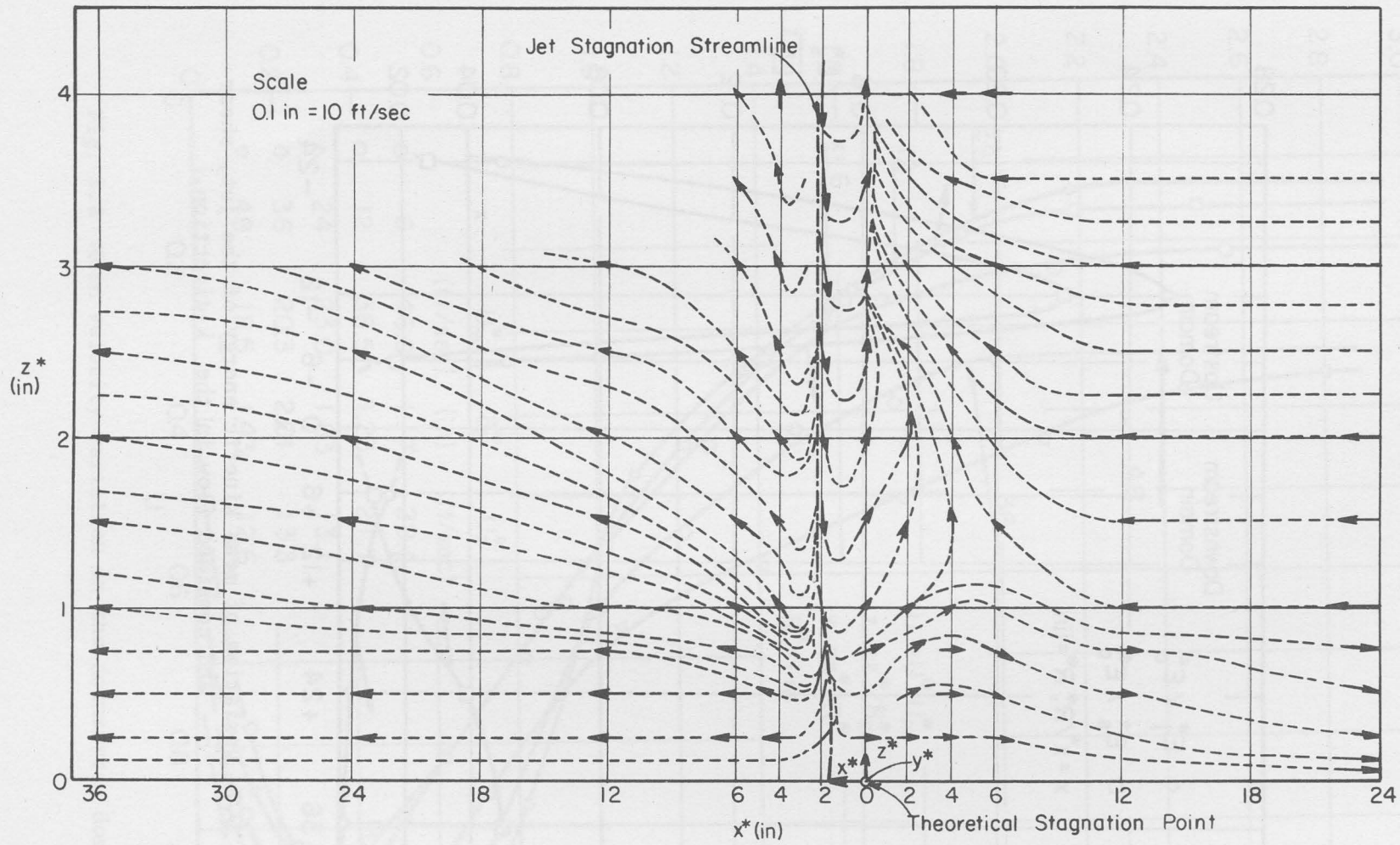

Fig. 5.6 Combined flow streamlines pattern.

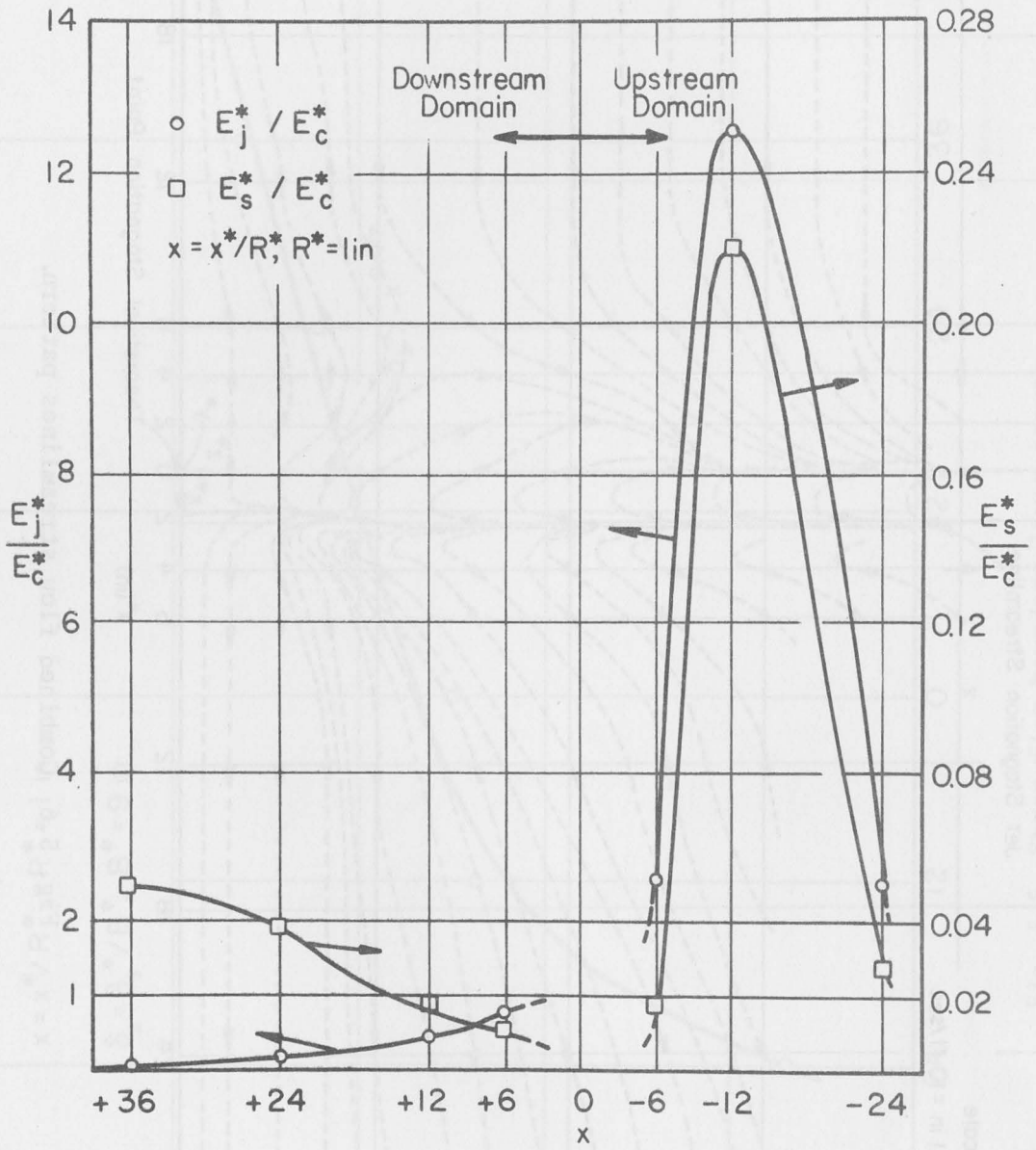

Fig. 5.7 Variation of mean kinetic energy of the jet, shear and combined flow in the x-direction.

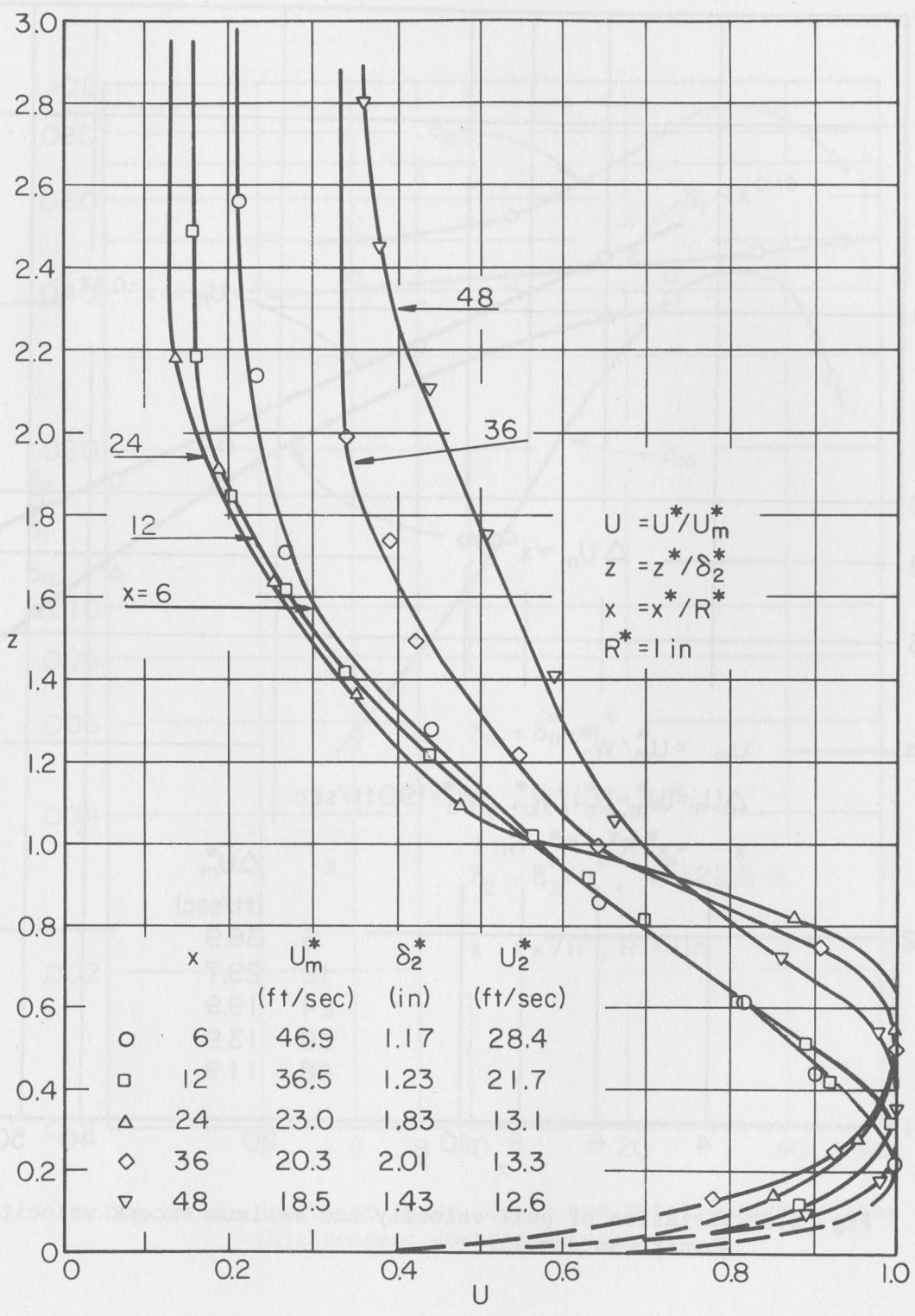

Fig. 5.8 Mean velocity variation in the downstream domain.

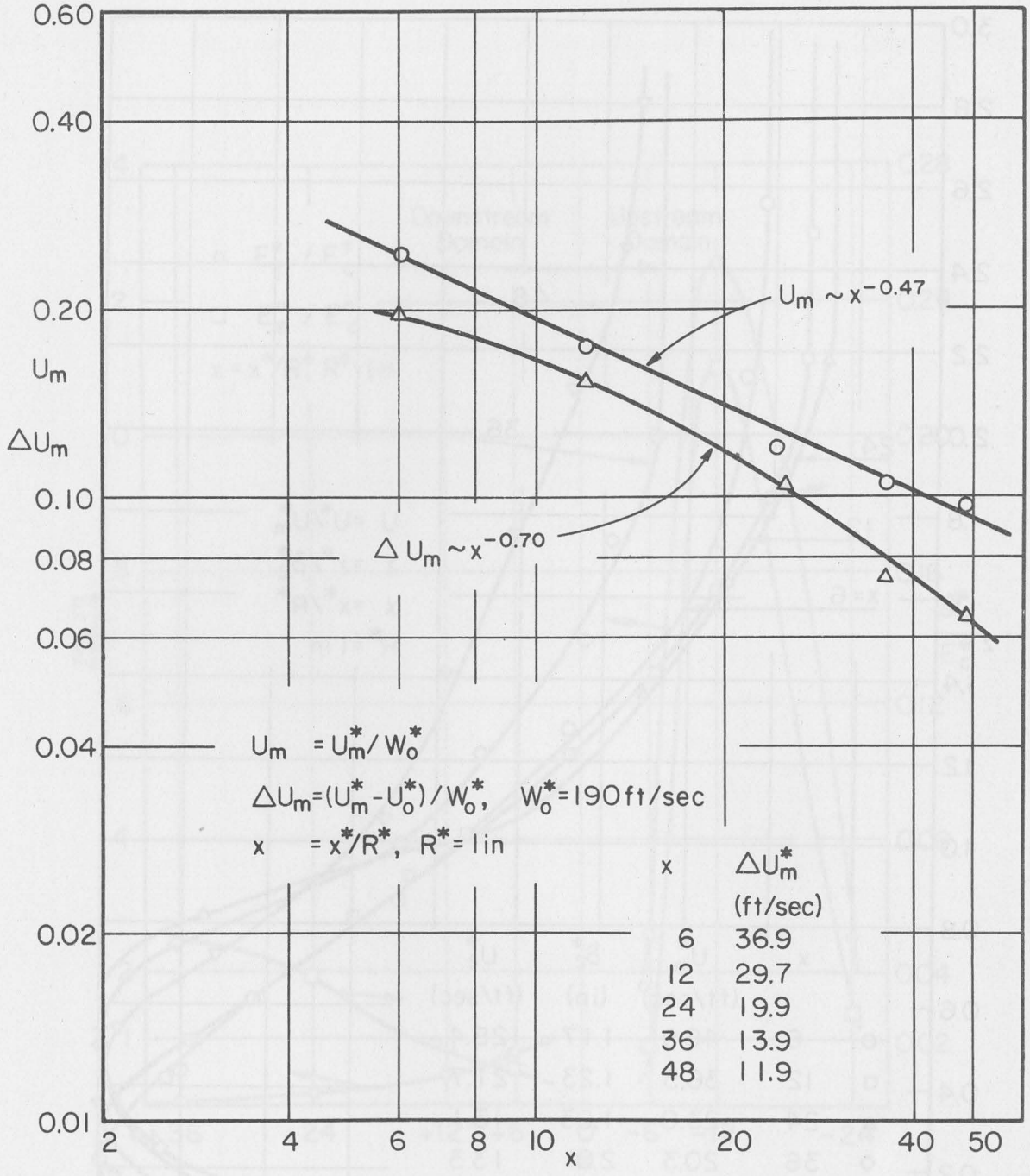

Fig. 5.9 Variation of peak velocity and maximum excess velocity; downstream domain.

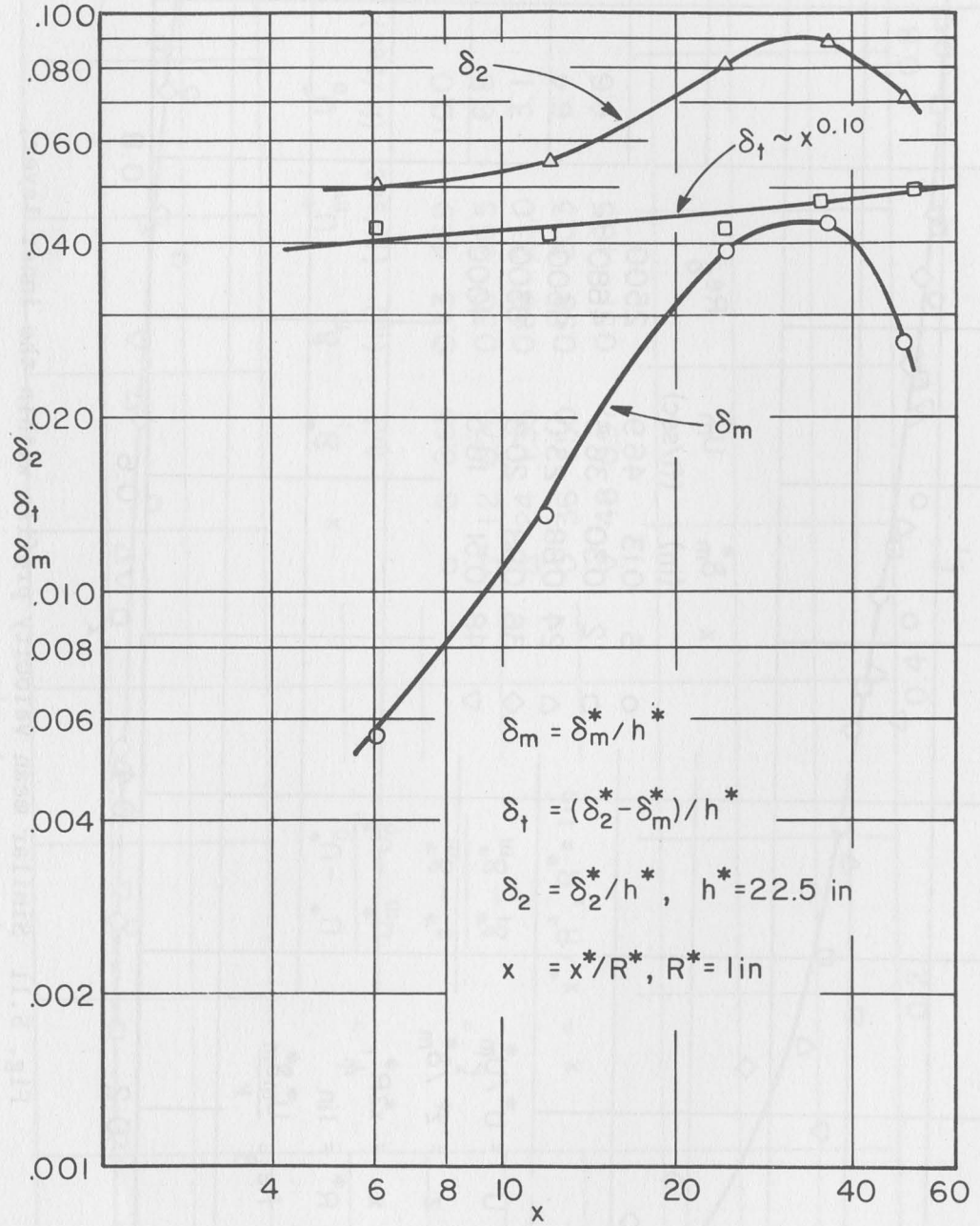

Fig. 5.10 Growth of inner, outer and total boundary layer thicknesses; downstream domain.

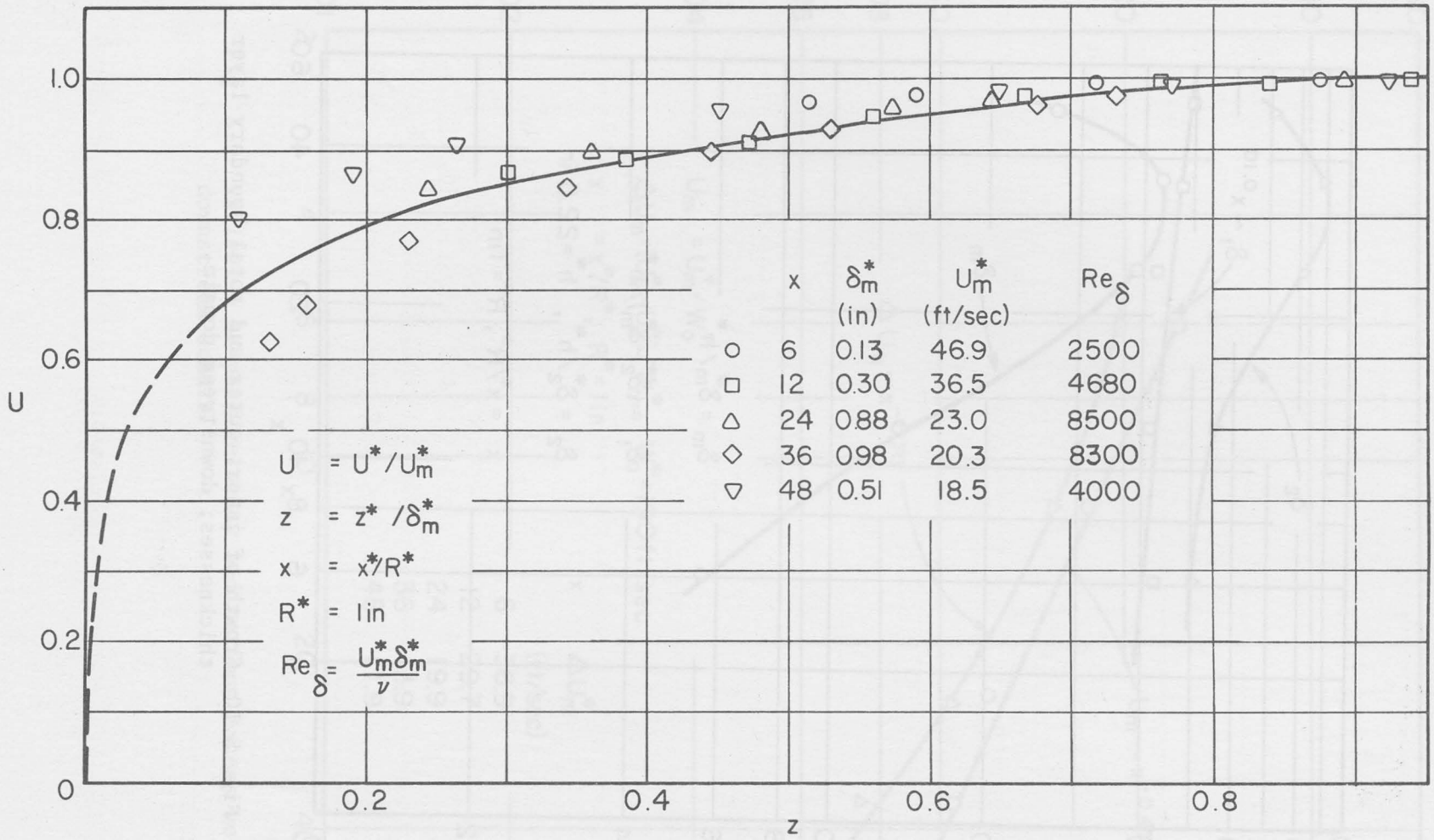

Fig. 5.11 Similar mean velocity profile within the inner layer; downstream domain.

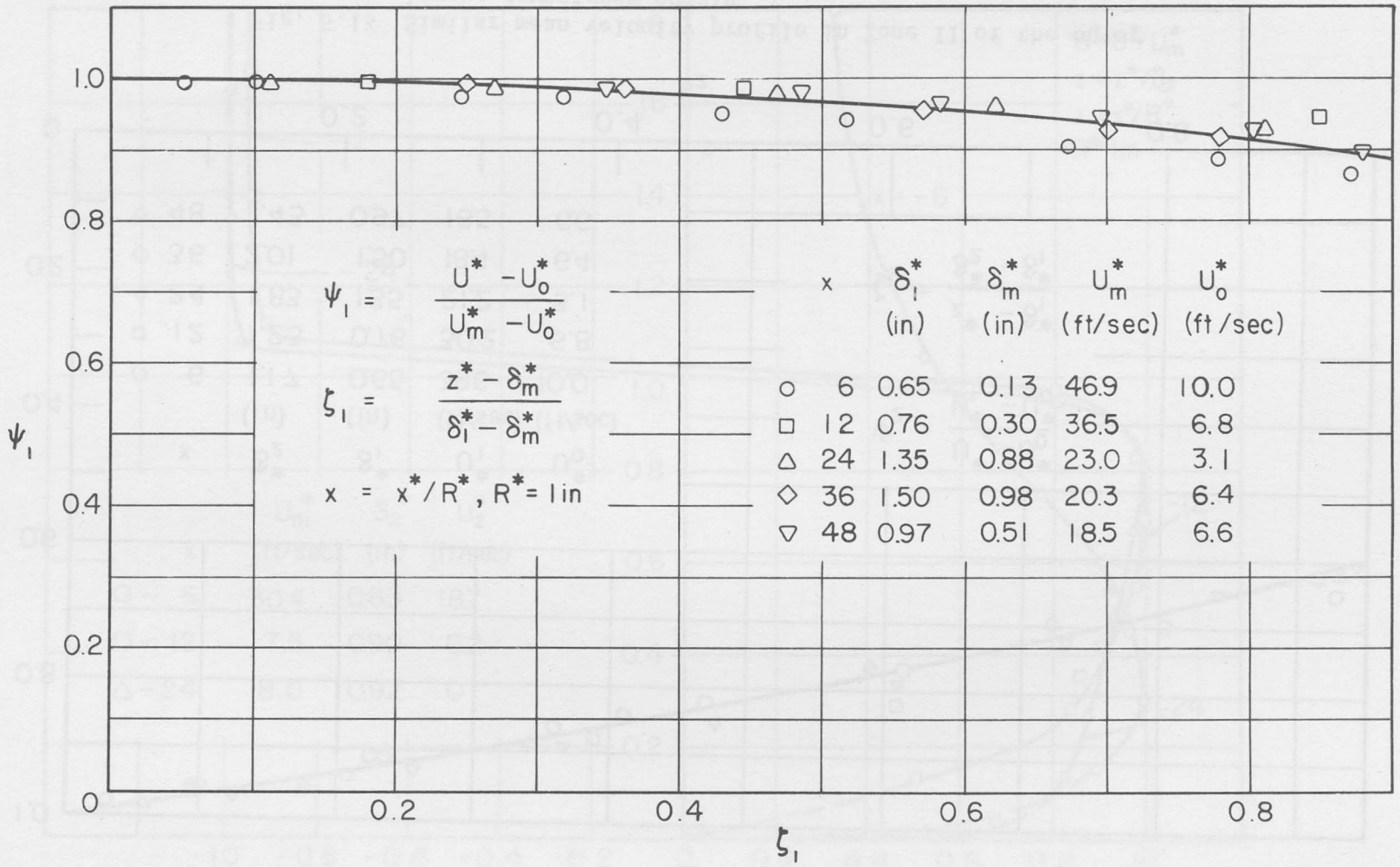

Fig. 5.12 Similar mean velocity profile in Zone I of the outer layer; downstream domain .

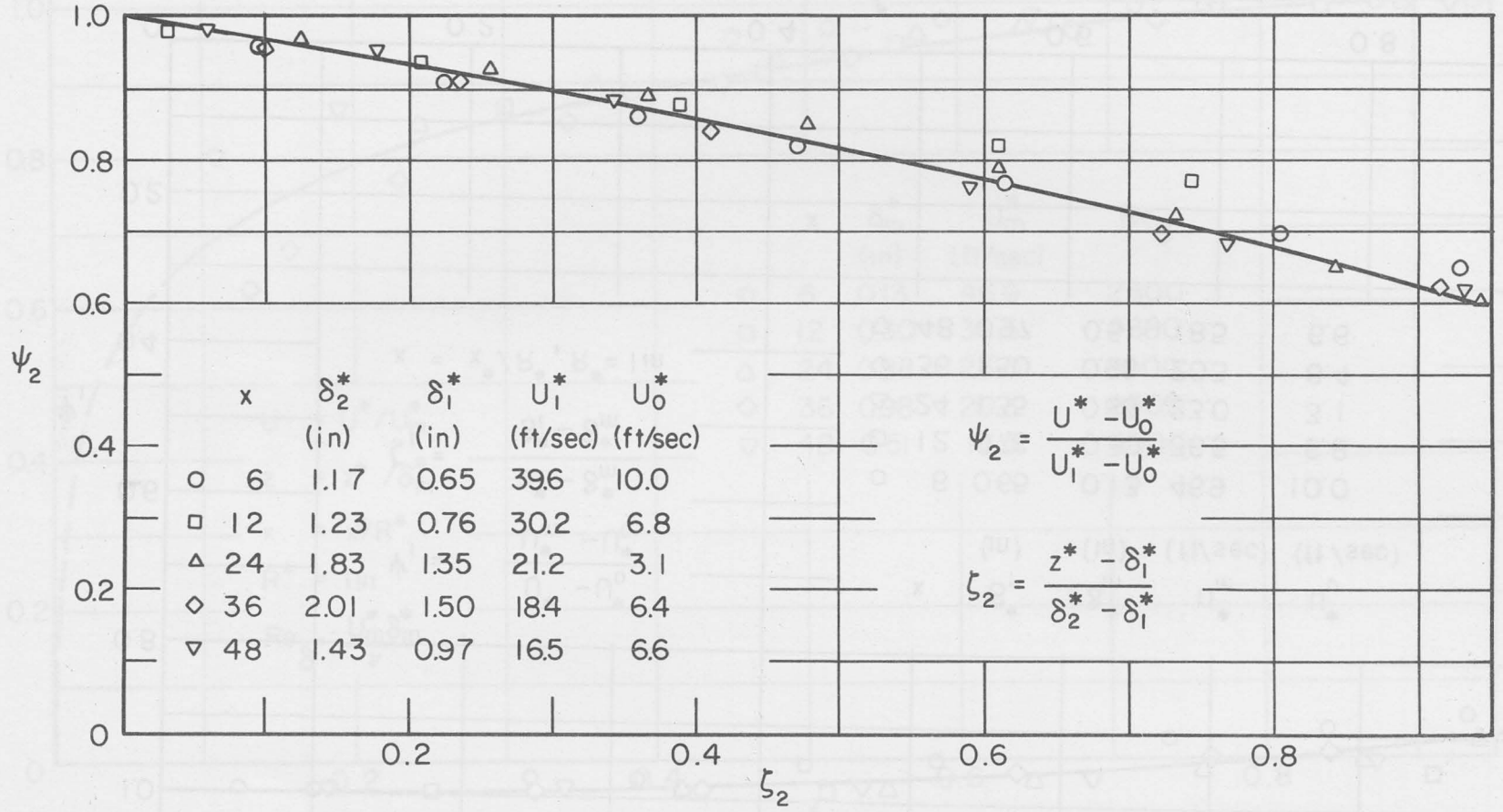

Fig. 5.13 Similar mean velocity profile in Zone II of the outer layer; downstream domain.

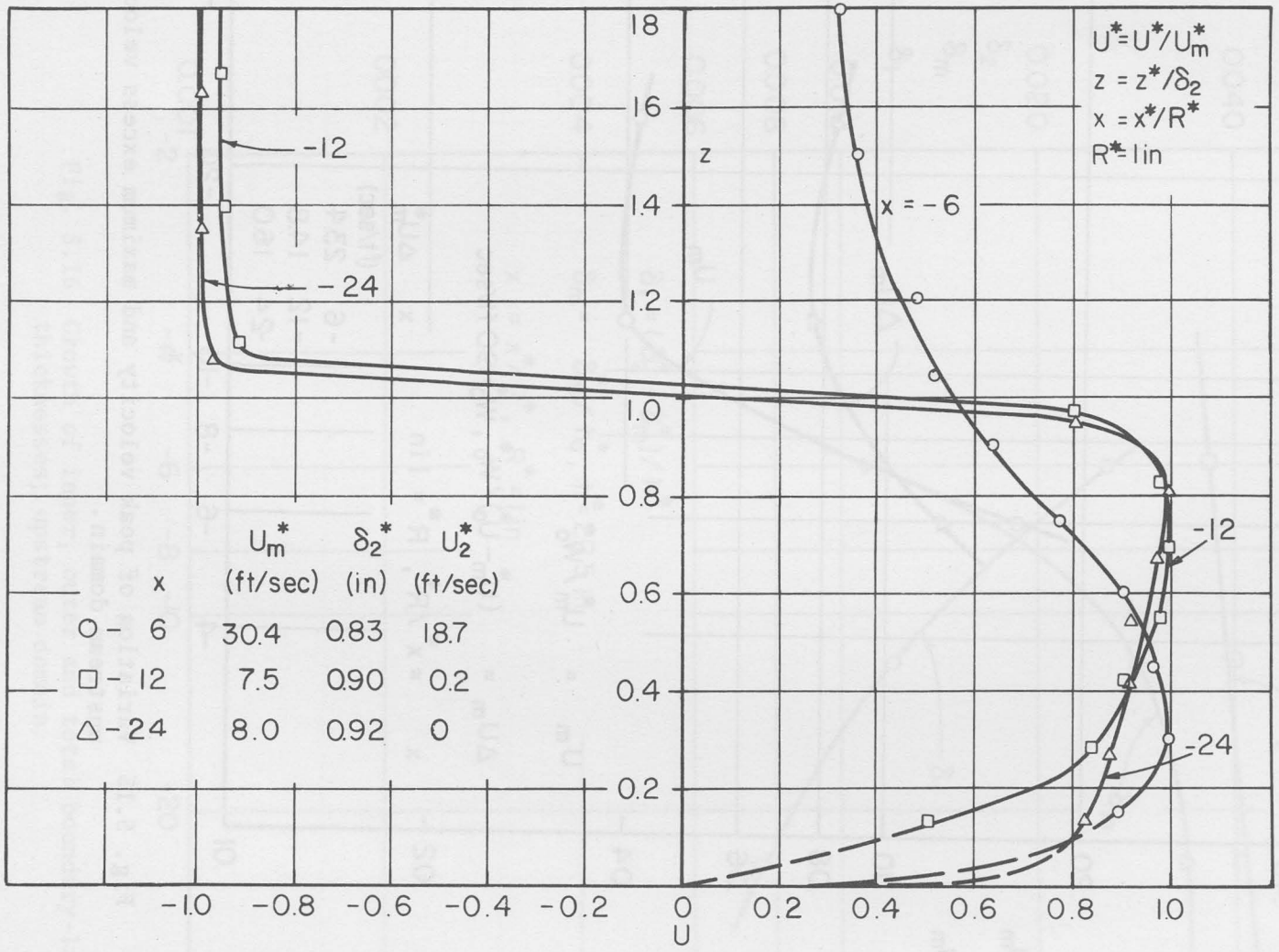

Fig. 5.14 Mean velocity variation in the upstream domain.

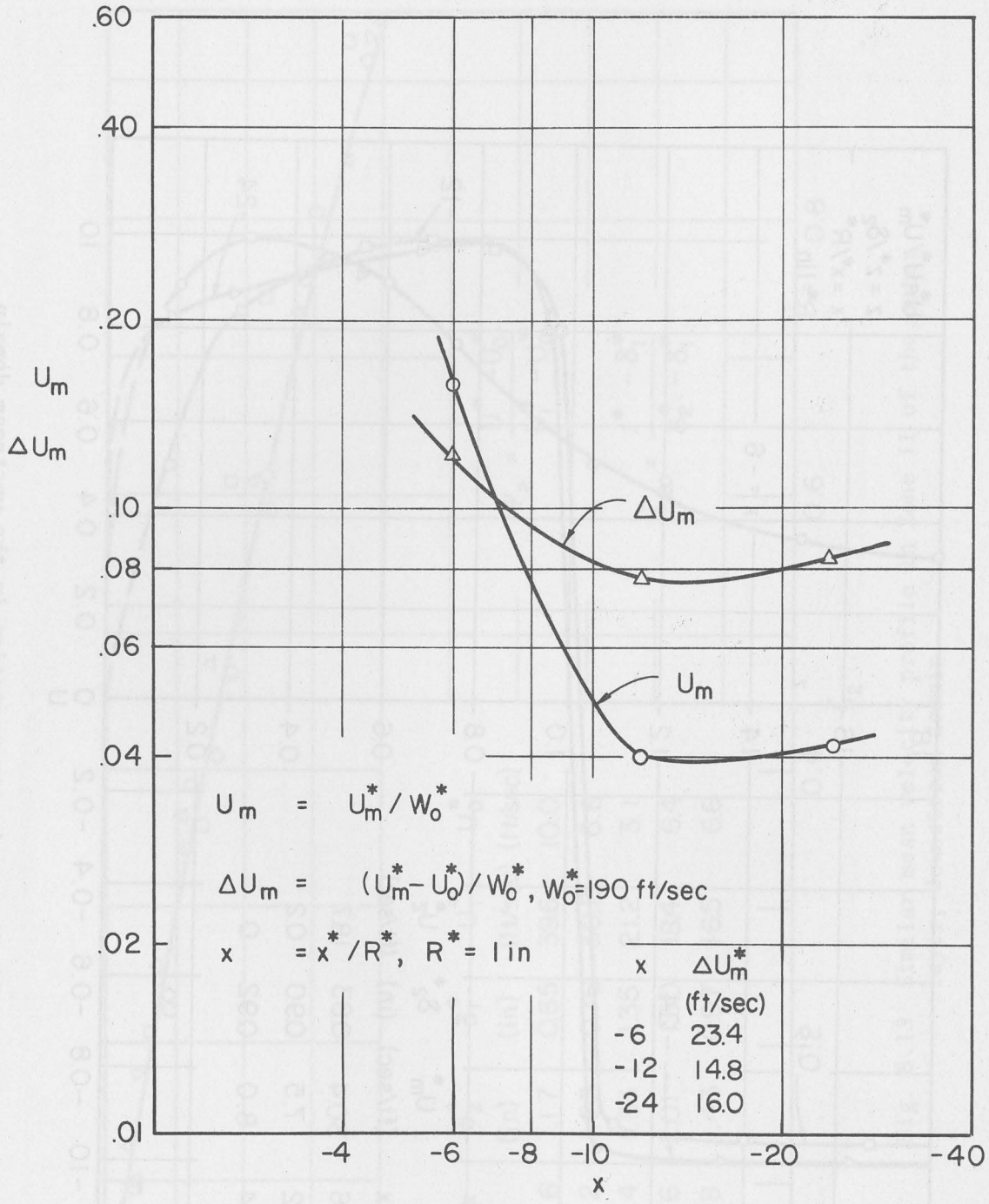

Fig. 5.15 Variation of peak velocity and maximum excess velocity; upstream domain.

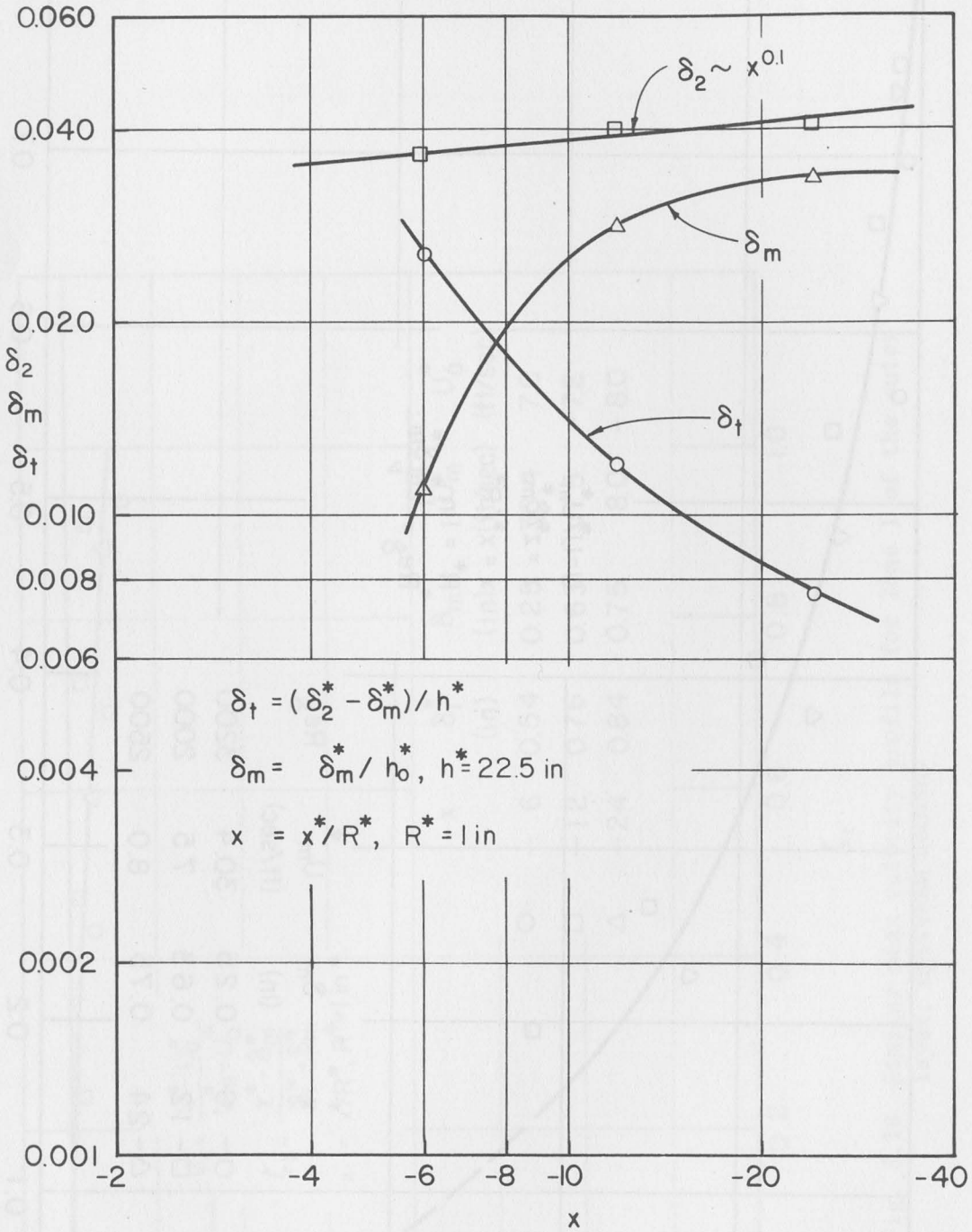

Fig. 5.16 Growth of inner, outer and total boundary-layer thicknesses; upstream domain.

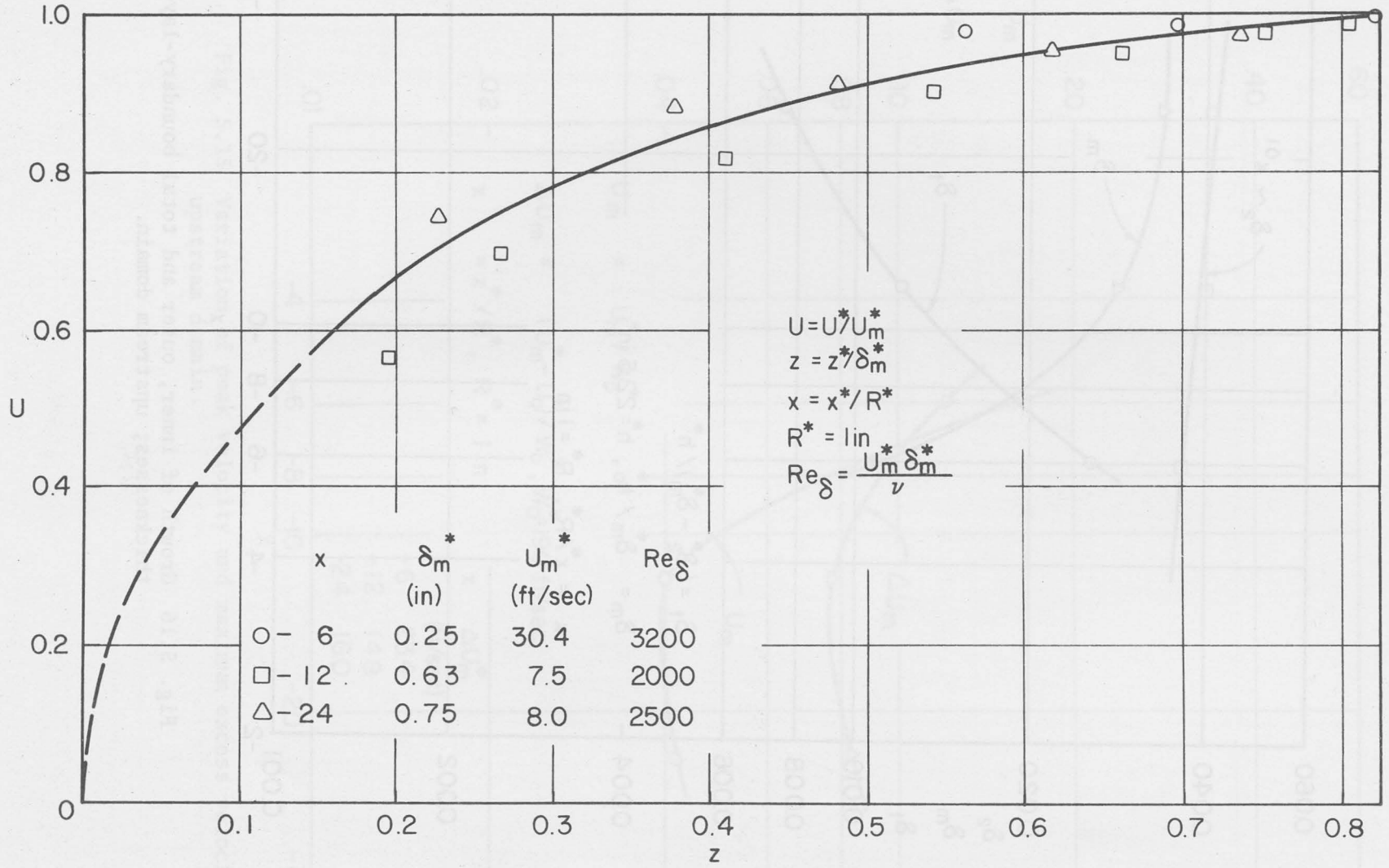

Fig. 5.17 Similar mean velocity profile within the inner layer; upstream domain.

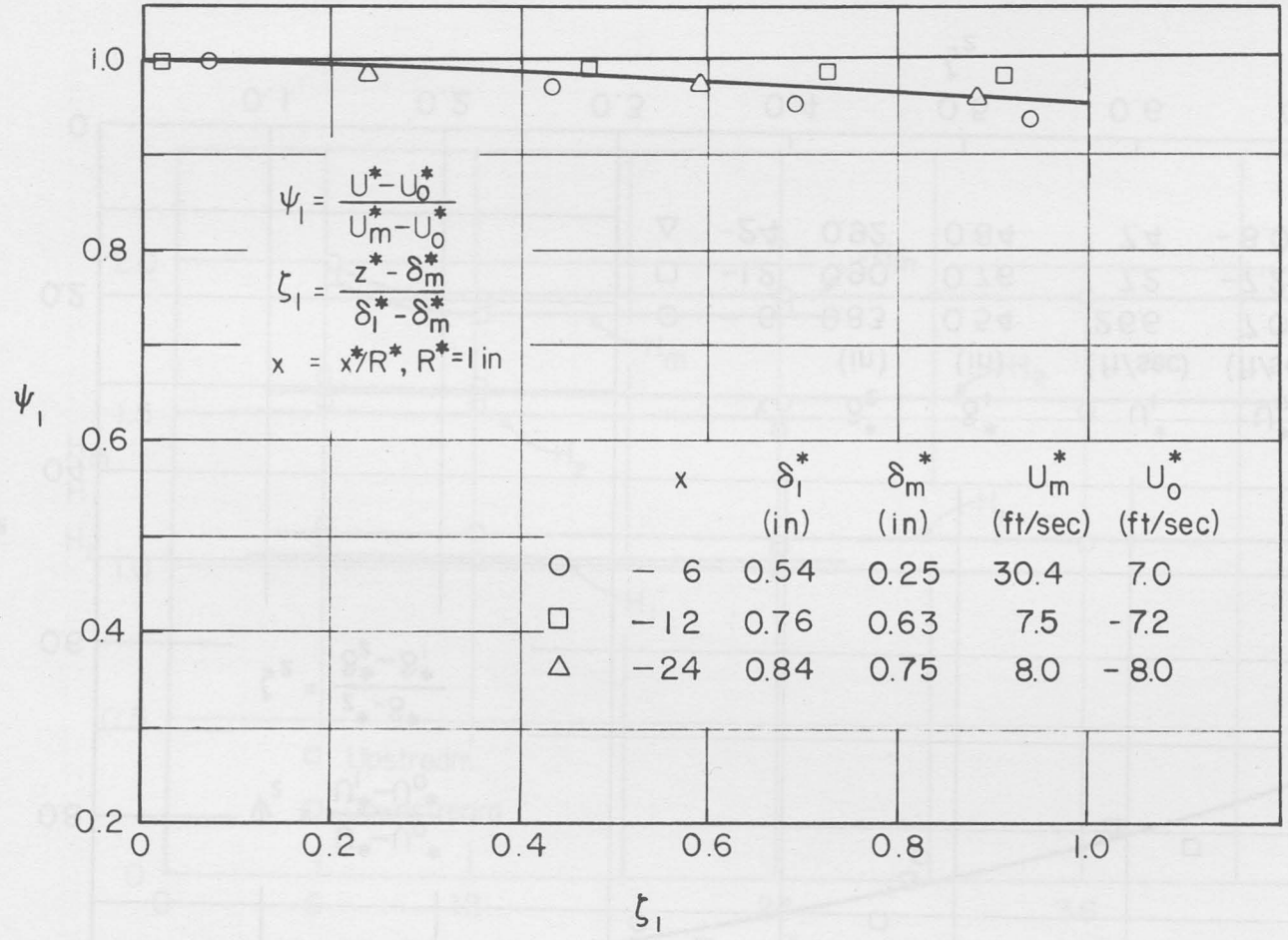

Fig. 5.18 Similar mean velocity profile for Zone I of the outer layer; upstream domain.

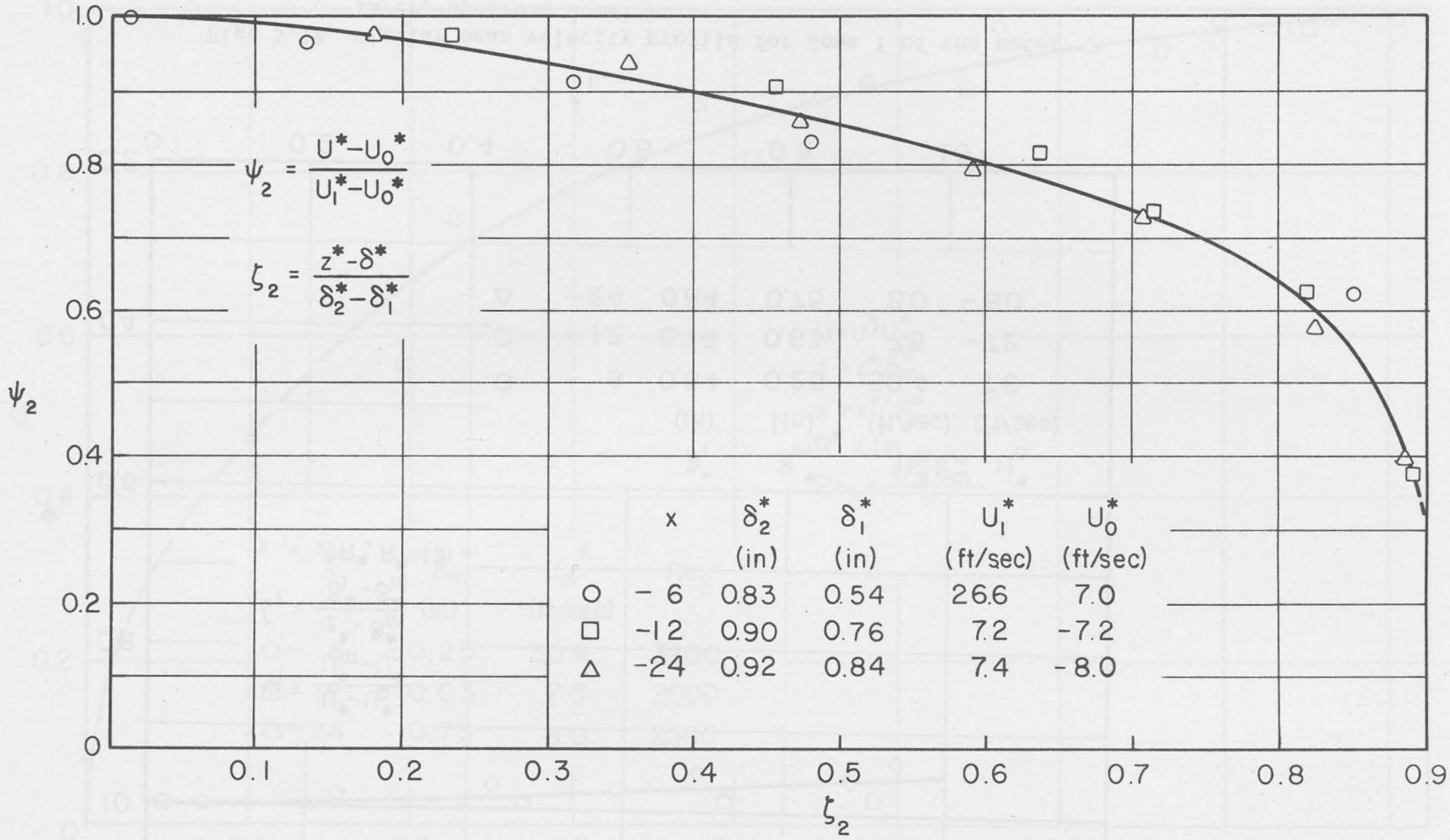

Fig. 5.19 Similar mean velocity profile for Zone II of the outer layer; upstream domain.

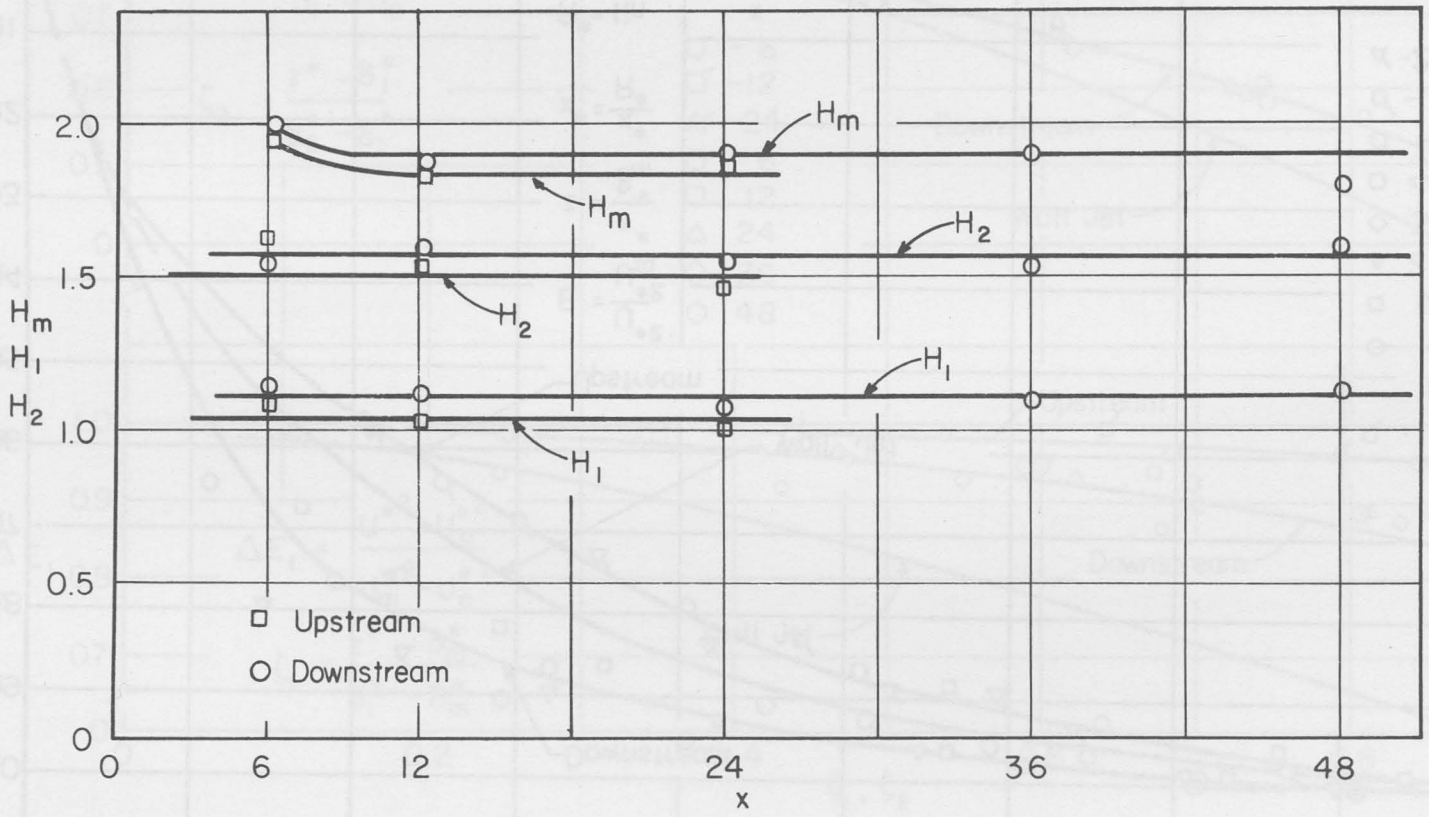

Fig. 5.20 Variation of the shape factor within the inner layer and the two zones of the outer layer for both flow domains.

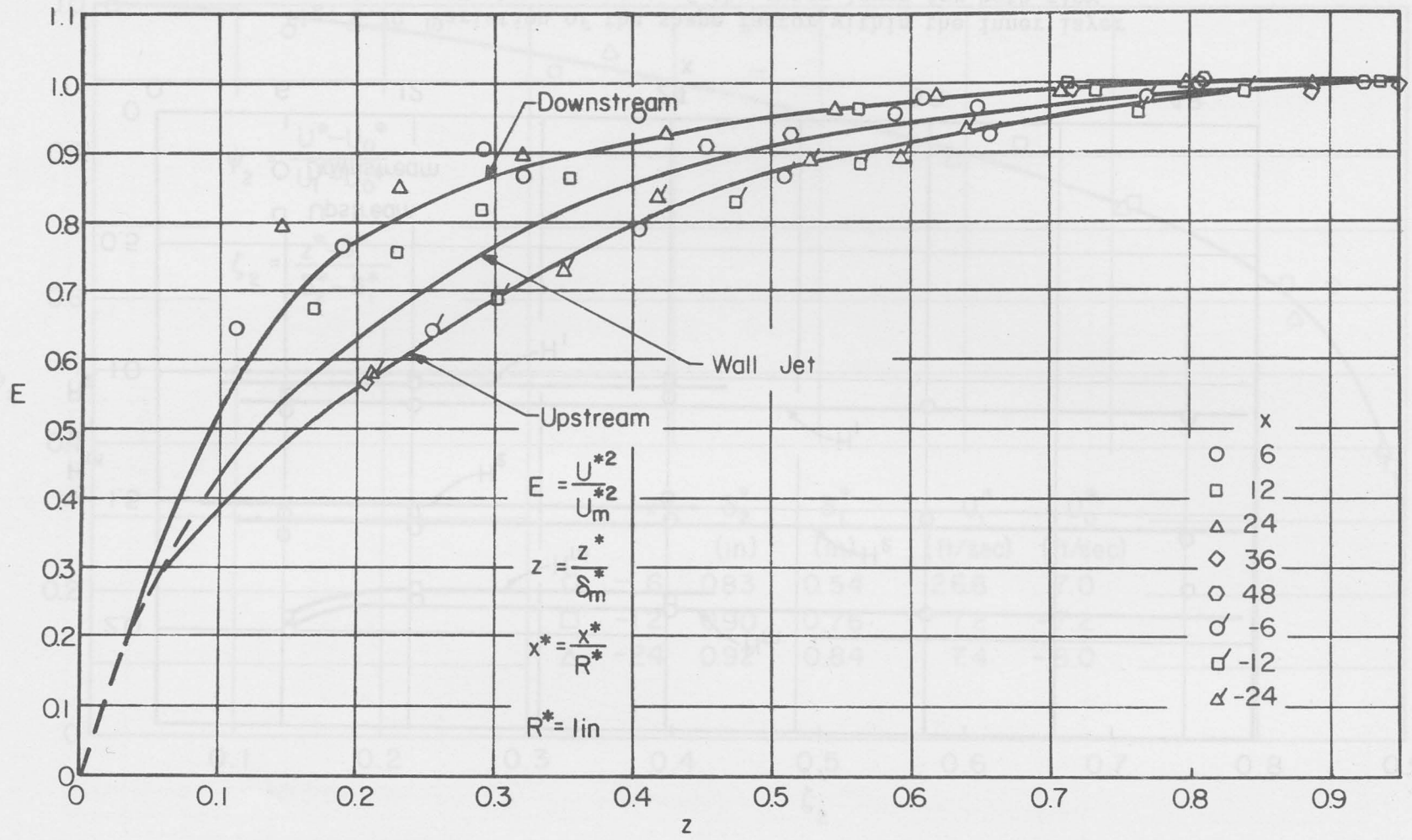

Fig. 5.21 Variation of mean kinetic energy in the inner layer for both flow domains.

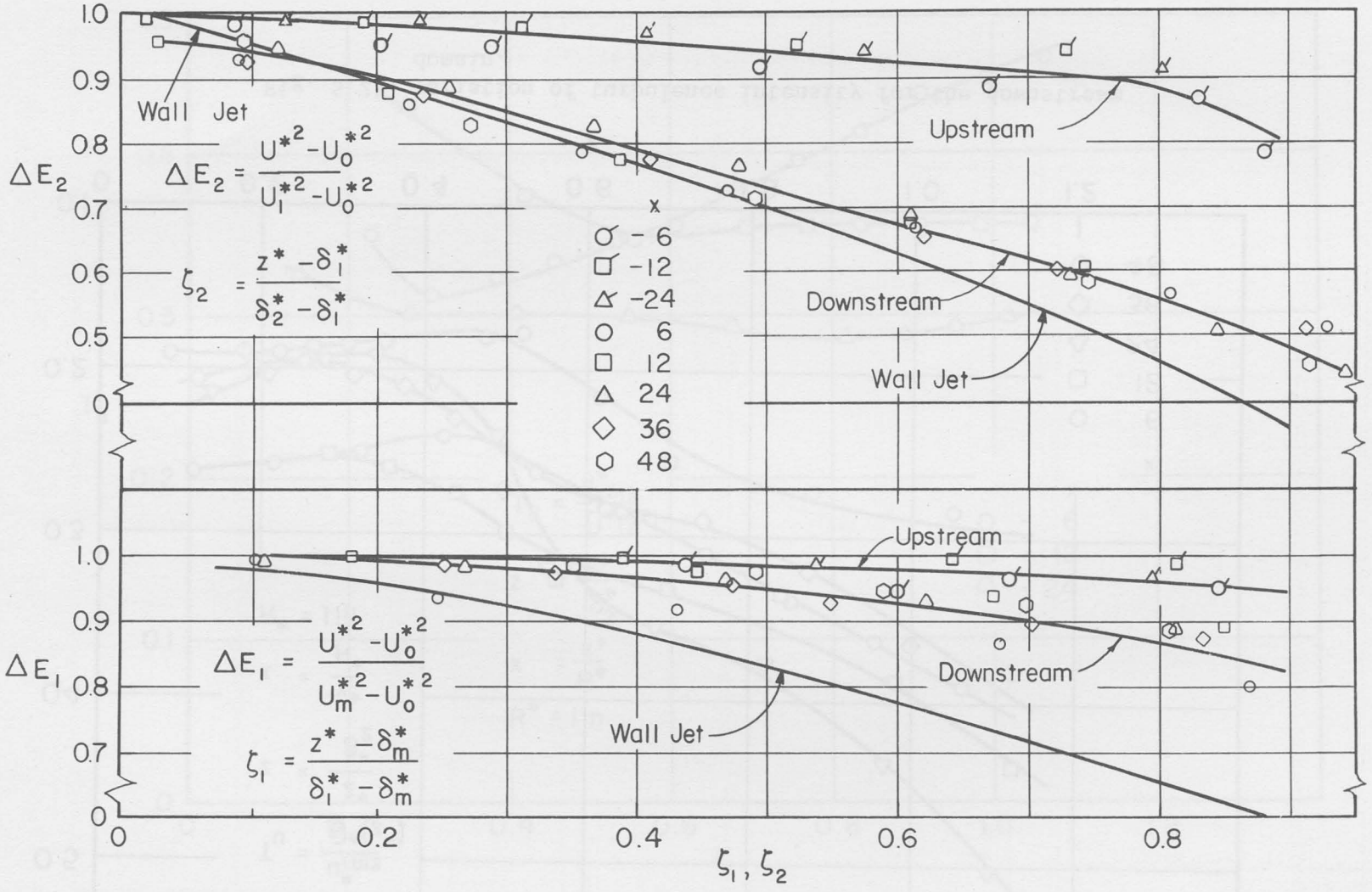

Fig. 5.22 Change of mean kinetic energy in the two zones of the outer layer for both flow domains.

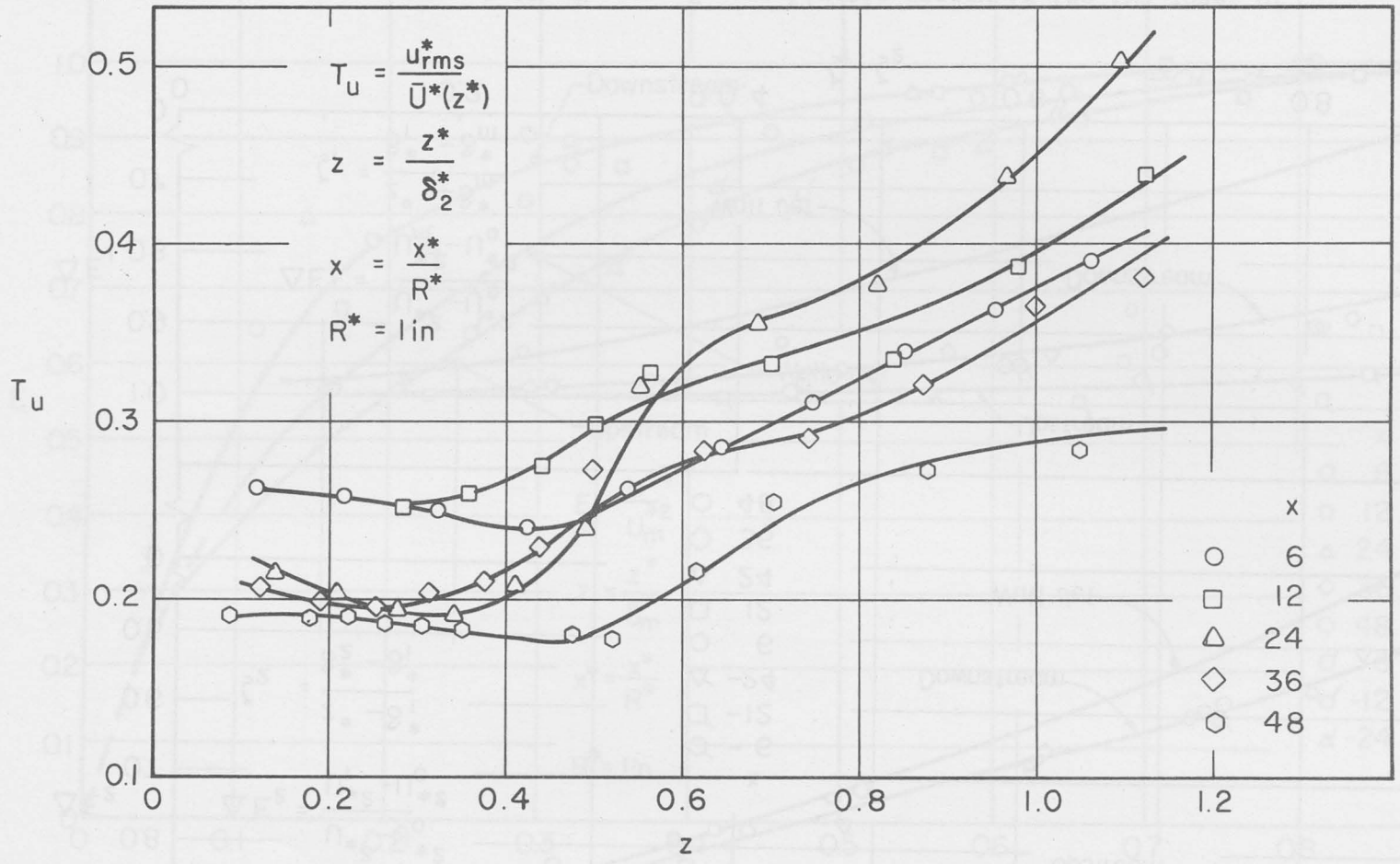

Fig. 5.23 Variation of turbulence intensity for the downstream domain.

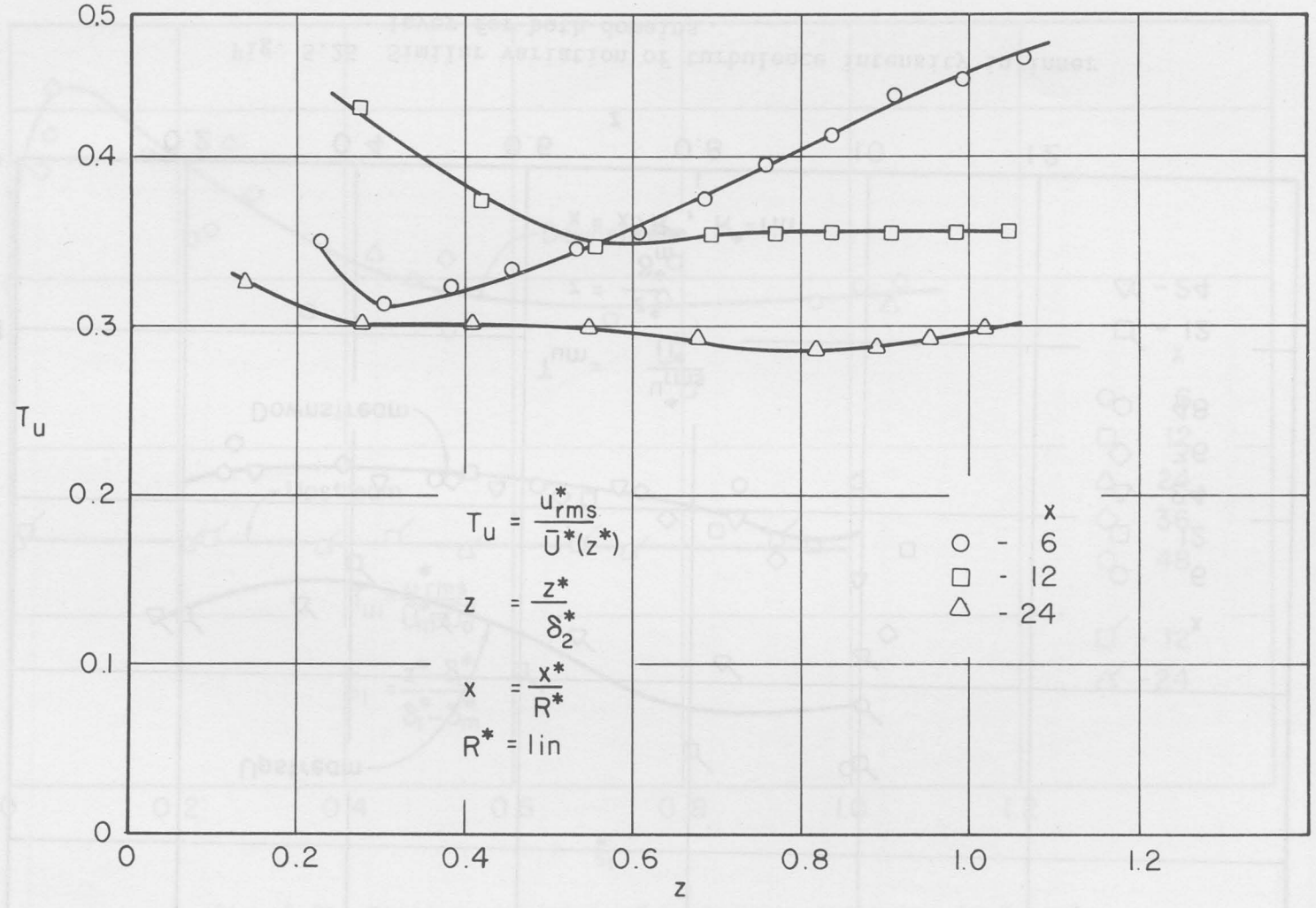

Fig. 5.24 Variation of turbulence intensity for the upstream domain.

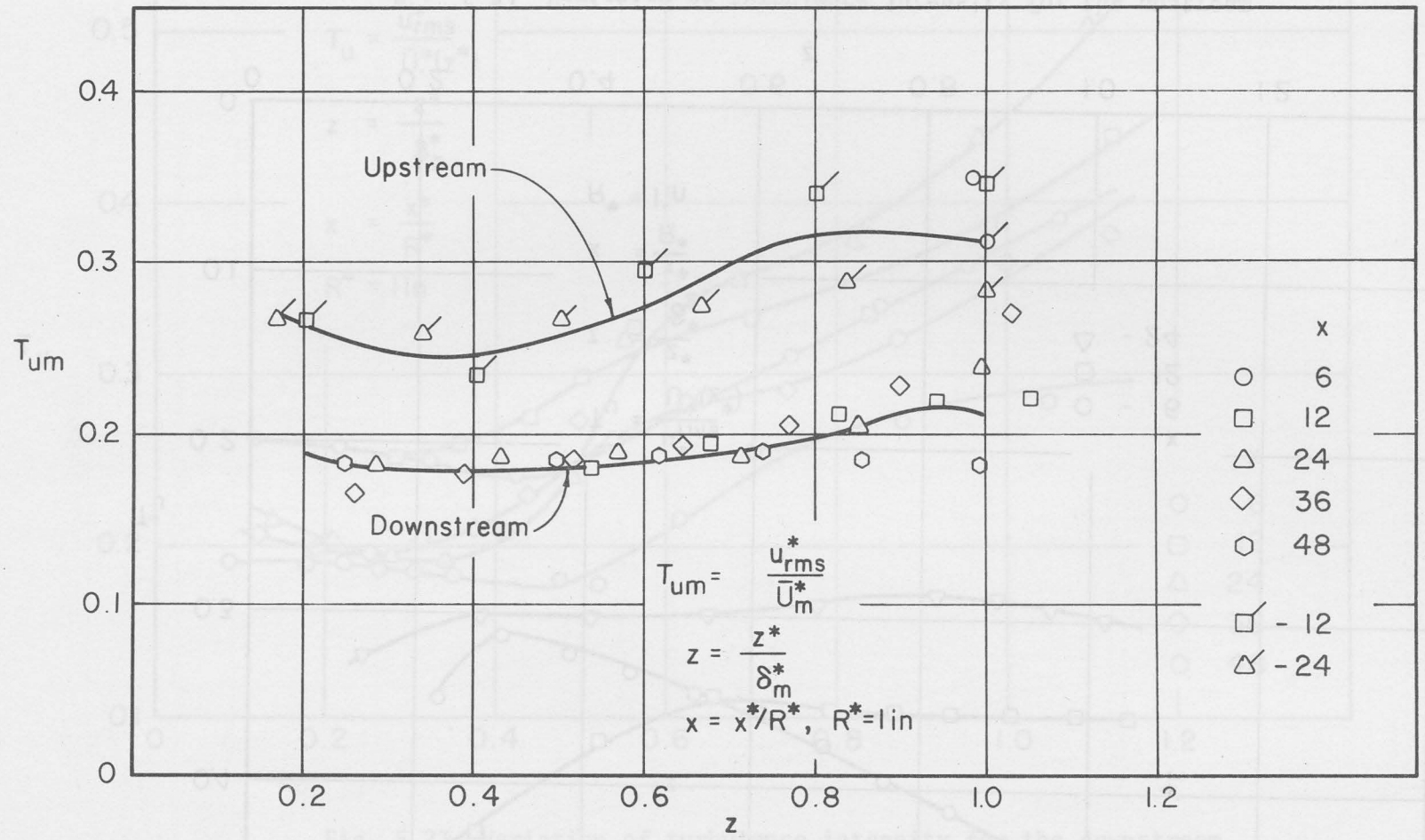

Fig. 5.25 Similar variation of turbulence intensity in inner layer for both domains.

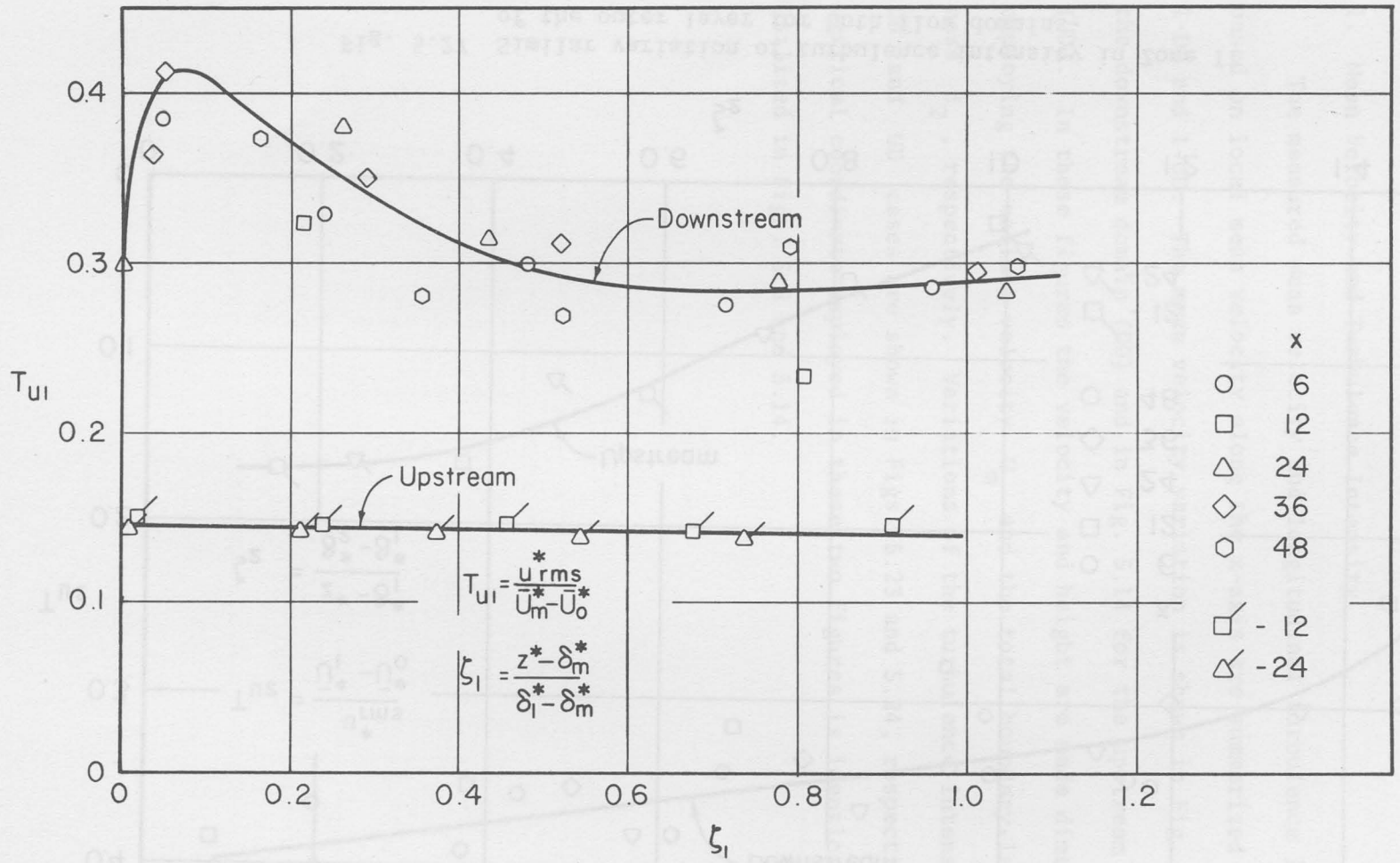

Fig. 5.26 Similar variation of turbulence intensity in Zone I of the outer layer for both domains.

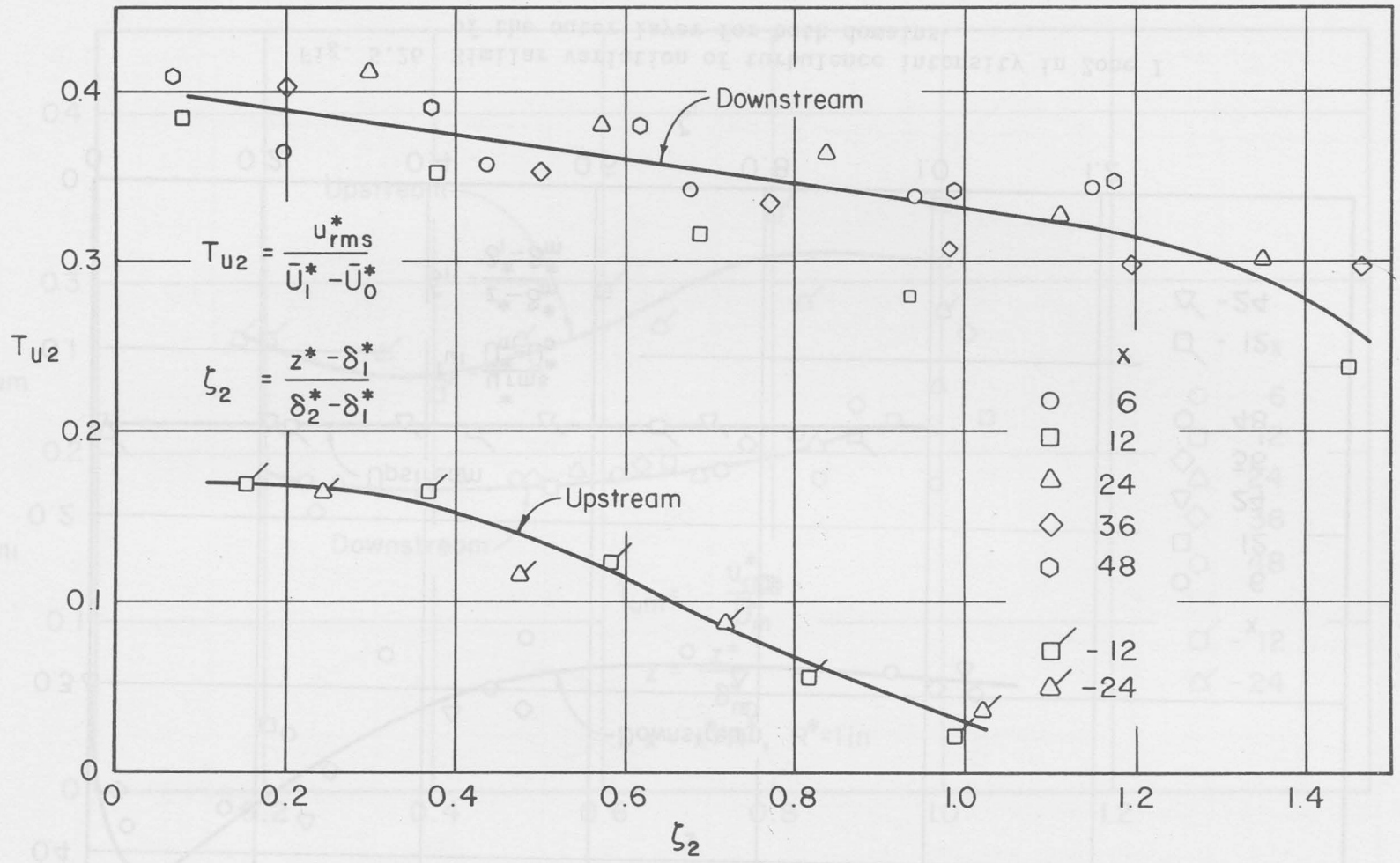

Fig. 5.27 Similar variation of turbulence intensity in Zone II of the outer layer for both flow domains.

APPENDIX

TABLES

1. Mean Velocity and Turbulence Intensity

The measured mean velocity and longitudinal turbulence intensity based on local mean velocity along the x-axis are summarized in Tables 1-DD and 1-UD. The mean velocity variation is shown in Fig. 5.8 for the downstream domain (DD) and in Fig. 5.14 for the upstream domain (UD). In these figures the velocity and height are made dimensionless employing the maximum velocity U_m and the total boundary-layer thickness δ_2, respectively. Variations of the turbulence intensity for DD and UD cases are shown in Figs. 5.23 and 5.24, respectively. The vertical coordinate employed in these two figures is identical to that utilized in Figs. 5.8 and 5.14.

TABLE 1 - DD

DOWNSTREAM DOMAIN

MEAN VELOCITY AND TURBULENCE INTENSITY

x*(in)	6			12			24			36			48		
	z* (in)	U* (ft/sec)	T_u	z* (in)	U* (ft/sec)	T_u	z* (in)	U* (ft/sec)	T_u	z* (in)	U* (ft/sec)	T_u	z* (in)	U* (ft/sec)	T_u
Inner Layer	0.0625	44.6	0.312	0.0625	27.2	0.215	0.0625	14.4	0.240	0.0625	8.2	0.228	0.0625	14.8	0.195
	0.1250	46.9	0.312	0.1250	32.3	0.195	0.1250	16.6	0.226	0.1250	12.3	0.216	0.1250	16.5	0.192
	0.1875	46.8	0.308	0.1875	35.3	0.200	0.1875	18.5	0.220	0.1875	14.4	0.213	0.1875	17.6	0.192
	0.2500	46.7	0.259	0.2500	36.4	0.205	0.2500	19.3	0.212	0.2500	15.8	1.209	0.2500	18.1	0.191
Outer Layer	0.3125	46.2	0.252	0.3000	36.5°	0.210°	0.3125	20.8	0.209	0.3125	17.1	0.205	0.3125	18.2	0.190
	0.3750	44.9	0.249	0.3125	36.4	0.211	0.3750	21.1	0.204	0.3750	17.9	0.201	0.3750	18.3	0.189
	0.4375	43.8	0.246	0.3750	36.0	0.215	0.4375	21.3	0.199	0.4375	18.4	0.200	0.4375	18.35	0.185
Zone I	0.5000	42.0	0.241	0.4375	35.4	0.219	0.5000	21.8	0.196	0.5000	18.7	0.200	0.5000	18.4	0.179
	0.5625	41.3	0.248	0.5000	34.1	0.226	0.5625	22.0	0.193	0.5625	19.2	0.201	0.5100	18.5°	0.179°
	0.6250	40.4	0.262	0.5625	33.6	0.227	0.6250	22.5	0.190	0.6250	19.4	0.202	0.5625	18.45	0.180
	0.6500	39.6°	0.270°	0.6250	32.3	0.228	0.6875	22.6	0.198	0.6875	19.7	0.207	0.6250	18.4	0.181
	0.6875	38.9	0.275	0.6875	31.5	0.231	0.7500	22.8	0.208	0.7500	19.8	0.210	0.6875	18.3	0.179
Outer Layer	0.7500	38.2	0.284	0.7500	29.5	0.232	0.8125	22.9	0.237	0.8125	19.9	0.219	0.7500	18.0	0.178
	0.8125	36.1	0.296	0.7600	29.2°	0.238°	0.8750	23.0	0.260	0.8750	20.0	0.230	0.8125	17.7	0.191
	0.8750	34.6	0.311	0.8125	28.9	0.261	0.9375	22.9	0.298	0.9375	20.2	0.255	0.8750	17.2	0.218
Zone II	0.9375	33.5	0.325	0.8750	27.5	0.288	1.0000	22.8	0.329	0.9750	20.3°	0.267°	0.9375	16.7	0.239
	1.0000	30.1	0.339	0.9375	26.7	0.324	1.1250	22.5	0.341	1.0000	20.2	0.274	0.9700	16.5°	0.248°
	1.1250	29.5	0.365	1.0000	25.3	0.350	1.2500	21.8	0.352	1.1250	20.1	0.278	1.0000	15.9	0.257
	1.1700	28.4°	0.370°	1.1250	23.1	0.358	1.3500	21.2°	0.355°	1.2500	19.7	0.281	1.1250	14.9	0.262
	U_o^* = 9.9 ft/sec at z^* = 3.0 in			1.2300	21.7°	0.362°	1.3750	20.9	0.366	1.3750	19.1	0.285	1.2500	14.1	0.269
				U_o^* = 6.8 ft/sec at z^* = 2.5 in			1.5000	20.0	0.377	1.5000	18.3	0.289	1.3750	13.4	0.274
							1.6250	17.7	0.404	1.6250	17.2	0.307	1.4300	12.6°	0.279°
							1.7500	13.4	0.439	1.7500	15.7	0.322	U_o^* = 6.6 ft/sec at z^* = 4.0 in		
							1.8300	13.1°	0.461°	1.8750	14.5	0.346			
							U_o^* = 3.1 ft/sec at z^* = 4.0 in			2.0000	13.6	0.367			
										2.0100	13.3°	0.370°			
										U_o^* = 6.4 ft/sec at z^* = 4.0 in					

TABLE 1 - UD

UPSTREAM DOMAIN

MEAN VELOCITY AND TURBULENCE INTENSITY

x*(in)	-6			-12			-24		
	z* (in)	U* (ft/sec)	T_u	z* (in)	U* (ft/sec)	T_u	z* (in)	U* (ft/sec)	T_u
	0.0625	26.2	0.312	0.0625	1.64	0.427	0.0625	1.64	0.338
Inner Layer	0.1250	29.5	0.293	0.1250	3.80	0.489	0.1250	6.65	0.325
	0.1875	30.0	0.306	0.1875	5.41	0.441	0.1875	6.85	0.313
	0.2500	30.4	0.311	0.2500	6.40	0.428	0.2500	6.95	0.301
	0.3125	30.0	0.323	0.3125	6.60	0.401	0.3125	7.22	0.300
Outer Layer	0.3750	29.7	0.334	0.3750	6.90	0.373	0.3750	7.35	0.300
	0.4375	28.8	0.345	0.4375	7.30	0.360	0.4375	7.40	0.300
Zone I	0.5000	27.6	0.357	0.5000	7.40	0.348	0.5000	7.42	0.299
	0.5400	26.6°	0.368°	0.5625	7.45	0.351	0.5625	7.57	0.295
	0.5625	25.7	0.376	0.6250	7.50	0.354	0.6250	7.65	0.292
Outer Layer	0.6250	24.1	0.397	0.6875	7.45	0.356	0.6875	7.95	0.287
	0.6875	21.8	0.417	0.7500	7.40	0.359	0.7500	8.00	0.284
Zone II	0.7500	19.3	0.437	0.7600	7.20°	0.358°	0.8125	7.61	0.288
	0.8125	18.8	0.447	0.8125	5.10	0.358	0.8400	7.40°	0.290°
	0.8300	18.7°	0.450°	0.8750	3.30	0.358	0.8750	6.60	0.293
	U_o^* = 7.1 ft/sec at z^* = 2.0 in			0.9000	0.20°	0.358°	0.9200	0.00	0.297
				U_o^* = -7.3 ft/sec at z^* = 1.5 in			U_o^* = -8.0 ft/sec at z^* = 1.5 in		

° - interpolated values

2. Integral Parameters

The displacement thickness Δ^*, momentum thickness θ^* and shape factor H for the three regions of the combined flow within both downstream and upstream domains are tabulated in Table 2. The results for the shape factor are shown in Fig. 5.20.

TABLE 2

INTEGRAL PARAMETERS

		INNER LAYER			OUTER LAYER ZONE I			OUTER LAYER ZONE II		
	x	Δ_m^* (in)	θ_m^* (in)	H_m	Δ_1^* (in)	θ_1^* (in)	H_1	Δ_2^* (in)	θ_2^* (in)	H_2
	6	0.00262	0.00132	1.982	0.0292	0.0262	1.114	1.493	0.965	1.55
	12	0.01602	0.00850	1.879	0.0054	0.0049	1.093	1.517	0.942	1.61
DD	24	0.01260	0.00665	1.895	0.0035	0.0034	1.021	0.993	0.645	1.54
	36	0.01600	0.00865	1.851	0.0154	0.0145	1.057	0.805	0.526	1.53
	48	0.00386	0.00211	1.828	0.0150	0.0141	1.066	1.083	0.674	1.61
	-24	0.00830	0.00460	1.802	0.0650	0.0645	1.005	0.0107	0.0075	1.48
UD	-12	0.01408	0.00770	1.822	0.0090	0.0089	1.017	0.0776	0.0051	1.52
	-6	0.00286	0.00147	1.939	0.0089	0.0083	1.067	0.8540	0.5180	1.65

April 1971

DISTRIBUTION LIST FOR UNCLASSIFIED
TECHNICAL REPORTS ISSUED UNDER
CONTRACT N00014-68-A TASK 000-414
0493-0001

Defense Documentation Center
Cameron Station
Alexandria, Virginia 22314 (12)

Technical Library
Naval Ship Research and Development Laboratory
Annapolis, Maryland 21402

Professor Bruce Johnson
Engineering Department
Naval Academy
Annapolis, Maryland 21402

Library
Naval Academy
Annapolis, Maryland 21402

Professor W.R. Debler
Department of Engineering Mechanics
University of Michigan
Ann Arbor, Michigan 48108

Professor W.P. Graebel
Department of Engineering Mechanics
University of Michigan
College of Engineering
Ann Arbor, Michigan 48108

Professor Finn C. Michelsen
Naval Architecture and Marine Engineering
445 West Engineering Building
University of Michigan
Ann Arbor, Michigan 48108

Dr. Francis Ogilvie
Department of Naval Architecture and Marine Engineering
University of Michigan
Ann Arbor, Michigan 48108

Professor W.W. Willmarth
Department of Aerospace Engineering
University of Michigan
Ann Arbor, Michigan 48108

Dr. S.A. Piacsek
Argonne National Laboratory
Applied Mathematics Division
9700 S. Cass Avenue
Argonne, Illinois 60439

AFOSR (REM)
1400 Wilson Boulevard
Arlington, Virginia 22204

Professor S. Corrsin
Mechanics Department
The Johns Hopkins University
Baltimore, Maryland 20910

Professor L.S.G. Kovasznay
The Johns Hopkins University
Baltimore, Maryland 20910

Professor O.M. Phillips
The Johns Hopkins University
Baltimore, Maryland 20910

Librarian
Department of Naval Architecture
University of California
Berkeley, California 94720

Professor Israel Cornet
Department of Mechanical Engineering
University of California
Berkeley, California 94720

Professor M. Holt
Division of Aeronautical Sciences
University of California
Berkeley, California 94720

Professor E.V. Laitone
Department of Mechanical Engineering
University of California
Berkeley, California 94720

Professor P. Lieber
Department of Mechanical Engineering
University of California
Institute of Engineering Research
Berkeley, California 94720

Professor J.R. Paulling
Department of Naval Architecture
University of California
Berkeley, California 94720

Professor J.V. Wehausen
Department of Naval Architecture
University of California
Berkeley, California 94720

Professor E.R. van Driest
Virginia Polytechnic Institute and University
Department of Aerospace Engineering
Blacksburg, Virginia 24061

Commander
Boston Naval Shipyard
Boston, Massachusetts 02129

Director
Office of Naval Research Branch Office
495 Summer Street
Boston, Massachusetts 02210

Commander
Puget Sound Naval Shipyard
Bremerton, Washington 98314

Professor J.J. Foody
Chairman, Engineering Department
State University of New York
Maritime College
Bronx, New York 10465

Dr. Alfred Ritter
Assistant Head, Applied Mechanics Department
Cornell Aeronautical Laboratory, Inc.
Buffalo, New York 14221

Dr. J.W. Morris
Manager, Material Sciences Section
Advanced Materials Research
Bell Aerospace Company
P.O. Box 1
Buffalo, New York 14240

Professor G.H. Carrier
Department of Engineering and Applied Physics
Harvard University
Cambridge, Massachusetts 02138

Commanding Officer
NROTC Naval Administrative Unit
Massachusetts Institute of Technology
Cambridge, Massachusetts 02139

Professor M.A. Abkowitz
Department of Naval Architecture and Marine Engineering
Massachusetts Institute of Technology
Cambridge, Massachusetts 02139

Professor A.T. Ippen
Department of Civil Engineering
Massachusetts Institute of Technology
Cambridge, Massachusetts 02139

Professor L.N. Howard
Department of Mathematics
Massachusetts Institute of Technology
Cambridge, Massachusetts 02139

Professor E.W. Merrill
Department of Mathematics
Massachusetts Institute of Technology
Cambridge, Massachusetts 02139

Professor E. Mollo-Christensen
Room 54-1722
Massachusetts Institute of Technology
Cambridge, Massachusetts 02139

Professor N. Newman
Department of Naval Architecture and Marine Engineering
Massachusetts Institute of Technology
Cambridge, Massachusetts 02139

Professor A.H. Shapiro
Department of Mechanical Engineering
Massachusetts Institute of Technology
Cambridge, Massachusetts 02139

Commander
Charleston Naval Shipyard
U.S. Naval Base
Charleston, South Carolina 29408

A.R. Kuhlthau, Director
Research Laboratories for the Engineering Sciences
Thorton Hall, University of Virginia
Charlottesville, Virginia 22903

Director
Office of Naval Research Branch Office
536 South Clark Street
Chicago, Illinois 60605

Library
Naval Weapons Center
China Lake, California 93555

Professor J.M. Burgers
Institute of Fluid Dynamics and Applied Mathematics
University of Maryland
College Park, Maryland 20742

Professor Pai
Institute for Fluid Dynamics and Applied Mathematics
University of Maryland
College Park, Maryland 20740

Acquisition Director
NASA Scientific & Technical Information
P.O. Box 33
College Park, Maryland 20740

Technical Library
Naval Weapons Laboratory
Dahlgren, Virginia 22448

Computation & Analyses Laboratory
Naval Weapons Laboratory
Dahlgren, Virginia 22448

Dr. C.S. Wells, Jr.
Manager - Fluid Mechanics
Advanced Technology Center, Inc.
P.O. Box 6144
Dallas, Texas 75222

Dr. R.H. Kraichnan
Dublin, New Hampshire 03444

Commanding Officer
Army Research Office
Box CM, Duke Station
Durham, North Carolina 27706

Professor A. Charnes
The Technological Institute
Northwestern University
Evanston, Illinois 60201

Dr. Martin H. Bloom
Polytechnic Institute of Brooklyn
Graduate Center, Dept. of Aerospace
Engineering and Applied Mechanics
Farmingdale, New York 11735

Technical Documents Center
Building 315
U.S. Army Mobility Equipment
Research and Development Center
Fort Belvoir, Virginia 22060

Professor J.E. Cermak
College of Engineering
Colorado State University
Ft. Collins, Colorado 80521

Technical Library
Webb Institute of Naval Architecture
Glen Cove, Long Island, New York 11542

Professor E.V. Lewis
Webb Institute of Naval Architecture
Glen Cove, Long Island, New York 11542

Dr. B.N. Pridmore Brown
Northrop Corporation
NORAIR-Div.
Hawthorne, California 90250

Dr. J.P. Breslin
Stevens Institute of Technology
Davidson Laboratory
Hoboken, New Jersey 07030

Dr. D. Savitsky
Stevens Institute of Technology
Davidson Laboratory
Hoboken, New Jersey 07030

Mr. C.H. Henry
Stevens Institute of Technology
Davidson Laboratory
Hoboken, New Jersey 07030

Dr. J.P. Craven
University of Hawaii
1801 University Avenue
Honolulu, Hawaii 96822

Professor E.L. Resler
Graduate School of Aeronautical Engineering
Cornell University
Ithaca, New York 14851

Professor John Miles
c/o I.G.P.P.
University of California, San Diego
La Jolla, California 92038

Director
Scrippe Institution of Oceanography
University of California
La Jolla, California 92037

Professor A. Ellis
University of California, San Diego
Department of Aerospace & Mechanical Engineering
La Jolla, California 92037

Dr. B. Sternlicht
Mechanical Technology Incorporated
968 Albany-Shaker Road
Latham, New York 12110

Dr. Coda Pan
Mechanical Technology Incorporated
968 Albany-Shaker Road
Latham, New York 12110

Mr. P. Eisenberg, President
Hydronautics, Inc.
Pindell School Road
Howard County
Laurel, Maryland 20810

Mr. M.P. Tulin
Hydronautics, Inc.
Pindell School Road
Howard County
Laurel, Maryland 20810

Mr. Alfonso Alcedan L.,Director
Laboratorio Nacional De Hydraulics
Antigui Cameno A. Ancon
Casilla Jostal 682
Lima, Peru

Commander
Long Beach Naval Shipyard
Long Beach, California 90802

Professor John Laufer
Department of Aerospace Engineering
University Park
Los Angeles, California 90007

Professor J.M. Killen
St. Anthony Falls Hydraulic Lab.
University of Minnesota
Minneapolis, Minnesota 55414

Lorenz G. Straub Library
St. Anthony Falls Hydraulic Lab.
Mississippi River at 3rd Avenue S.E.
Minneapolis, Minnesota 55414

Professor J. Ripkin
St. Anthony Falls Hydraulic Lab.
University of Minnesota
Minneapolis, Minnesota 55414

Dr. W. Silberman
St. Anthony Falls Hydraulic Lab.
Mississippi River at 3rd Avenue S.E.
Minneapolis, Minnesota 55414

Superintendent
Naval Postgraduate School
Library Code 0212
Monterey, California 93940

Professor A.B. Metzner
University of Delaware
Newark, New Jersey 19711

Technical Library
Naval Underwater Systems Center
Newport, Rhode Island 02840

Professor Dudley D. Fuller
Department of Mechanical Engineering
Columbia University
New York, New York 10027

Professor V. Castelli
Department of Mechanical Engineering
Columbia University
New York, New York 10027

Professor H. Elrod
Department of Mechanical Engineering
Columbia University
New York, New York 10027

Professor J.J. Stoker
Institute of Mathematical Sciences
New York University
251 Mercer Street
New York, New York 10003

Society of Naval Architects and Marine Engineering
74 Trinity Place
New York, New York 10006

Engineering Societies Library
345 East 47th Street
New York, New York 10017

Office of Naval Research
New York Area Office
207 W. 24th Street
New York, New York 10011

Miss O.M. Leach, Librarian
National Research Council
Aeronautical Library
Montreal Road
Ottawa 7, Canada

Technical Library
Naval Ship Research and Development Center
Panama City, Florida 32401

Technical Library
Naval Undersea R & D Center
Pasadena Laboratory
3202 E. Foothill Boulevard
Pasadena, California 91107

Dr. Andrew Fabula
Naval Undersea Research & Development Center
Pasadena Laboratory
3202 E. Foothill Boulevard
Pasadena, California 91107

Dr. J.W. Hoyt
Naval Undersea R & D Center
Pasadena Laboratory
3202 E. Foothill Boulevard
Pasadena, California 91107

Professor A. Acosta
Department of Mechanical Engineering
California Institute of Technology
Pasadena, California 91109

Professor H. Liepmann
Department of Aeronautics
California Institute of Technology
Pasadena, California 91109

Professor M.S. Plesset
Engineering Division
California Institute of Technology
Pasadena, California 91109

Professor A. Roshko
California Institute of Technology
Pasadena, California 91109

Professor T.Y. Wu
Department of Engineering
California Institute of Technology
Pasadena, California 91109

Director
Office of Naval Research Branch Office
1030 E. Green Street
Pasadena, California 91101

Naval Ship Engineering Center
Philadelphia Division
Technical Library
Philadelphia, Pennsylvania 19112

Technical Library
Philadelphia Naval Shipyard
Philadelphia, Pennsylvania 19112

Professor R.C. Mac Camy
Department of Mathematics
Carnegie Institute of Technology
Pittsburgh, Pennsylvania 15213

Dr. Paul Kaplan
Oceanics, Inc.
Plainview, Long Island, New York 11803

Technical Library
Naval Missile Center
Point Mugu, California 93441

Technical Library
Naval Civil Engineering Laboratory
Port Hueneme, California 93041

Commander
Portsmouth Naval Shipyard
Portsmouth, New Hampshire 03801

Commander
Norfolk Naval Shipyard
Portsmouth, Virginia 23709

Professor F.E. Bisshopp
Division of Engineering
Brown University
Providence, Rhode Island 02912

Dr. William A. Gross, Vice President
Ampex Corporation
401 Broadway
Redwood City, California 94063

Dr. H.N. Abramson
Southwest Research Institute
8500 Culebra Road
San Antonio, Texas 78228

Editor
Applied Mechanics Review
Southwest Research Institute
8500 Culebra Road
San Antonio, Texas 78206

Office of Naval Research
San Francisco Area Office
50 Fell Street
San Francisco, California 94102

Library
Pearl Harbor Naval Shipyard
Box 400
FPO San Francisco, California 96610

Technical Library
Hunters Point Naval Shipyard
San Francisco, California 94135

Librarian
Naval Ordnance Laboratory
White Oak
Silver Spring, Maryland 20910

Fenton Kennedy Document Library
The Johns Hopkins University
Applied Physics Laboratory
8621 Georgia Avenue
Silver Spring, Maryland 20910

Professor E.Y. Hsu
Department of Civil Engineering
Stanford University
Stanford, California 94305

Dr. Byrne Perry
Department of Civil Engineering
Stanford University
Stanford, California 94305

Dr. R.L. Street
Department of Civil Engineering
Stanford University
Stanford, California 94305

Professor Milton Van Dyke
Department of Aeronautical Engineering
Stanford University
Stanford, California 94305

Professor R.C. Di Prima
Department of Mathematics
Rensselaer Polytechnic Institute
Troy, New York 12180

Professor J. Lumley
Ordnance Research Laboratory
Pennsylvania State University
University Park, Pennsylvania 16801

Dr. M. Sevik
Ordnance Research Laboratory
Pennsylvania State University
University Park, Pennsylvania 16801

Dr. J.M. Robertson
Department of Theoretical and Applied Mechanics
University of Illinois
Urbana, Illinois 61803

Technical Library
Mare Island Naval Shipyard
Vallejo, California 94592

Code 438
Office of Naval Research
Department of the Navy
Arlington, Virginia 22217 (3)

Code 461
Office of Naval Research
Department of the Navy
Arlington, Virginia 22217

Code 463
Office of Naval Research
Department of the Navy
Arlington, Virginia 22217

Code 472
Office of Naval Research
Department of the Navy
Arlington, Virginia 22217

Code 468
Office of Naval Research
Department of the Navy
Arlington, Virginia 22217

Code 473
Office of Naval Research
Department of the Navy
Arlington, Virginia 22217

Code 481
Office of Naval Research
Department of the Navy
Arlington, Virginia 22217

Code 2627
Naval Research Laboratory
Washington, D.C. 20390 (6)

Library, Code 2620 (ONRL)
Naval Research Laboratory
Washington, D.C. 20390 (6)

Code 6170
Naval Research Laboratory
Washington, D.C. 20390

Code 4000
Director of Research
Naval Research Laboratory
Washington, D.C. 20390

Code 8030 (Maury Center)
Naval Research Laboratory
Washington, D.C. 20390

Code 8040
Naval Research Laboratory
Washington, D.C. 20390

Code 031
Naval Ship Systems Command
Washington, D.C. 20390

Code 0341
Naval Ship Systems Command
Washington, D.C. 20390

Code 03412B (L. Benen)
Naval Ship Systems Command
Washington, D.C. 20390

Code 03412 (J. Schuler)
Naval Ship Systems Command
Washington, D.C. 20390

Code 2052
Naval Ship Systems Command
Washington, D. C. 20390

Code 6034
Naval Ship Engineering Center
Center Building
Prince George's Center
Hyattsville, Maryland 20782

Code 6110
Naval Ship Engineering Center
Center Building
Prince George's Center
Hyattsville, Maryland 20782

Code 6113
Naval Ship Engineering Center
Center Building
Prince George's Center
Hyattsville, Maryland 20782

Code 6114
Naval Ship Engineering Center
Center Building
Prince George's Center
Hyattsville, Maryland 20782

Code 6120E
Naval Ship Engineering Center
Center Building
Prince George's Center
Hyattsville, Maryland 20782

Code 6136
Naval Ship Engineering Center
Center Building
Prince George's Center
Hyattsville, Maryland 20782

Dr. A. Powell
Code 01
Naval Ship Research and Development Center
Washington, D.C. 20034

Mr. W.M. Ellsworth
Code 0H50
Naval Ship Research and Development Center
Washington, D.C. 20034

Central Library
Code L42
Naval Ship Research and Development Center
Washington, D.C. 20034

Dr. W.E. Cummins
Code 500
Naval Ship Research and Development Center
Washington, D.C. 20034

Mr. S.F. Crump
Code 513
Naval Ship Research and Development Center
Washington, D.C. 20034

Mr. R. Wermter
Code 520
Naval Ship Research and Development Center
Washington, D.C. 20034

Dr. P. Pien
Code 521
Naval Ship Research and Development Center
Washington, D.C. 20034

Dr. W.B. Morgan
Code 540
Naval Ship Research and Development Center
Washington, D.C. 20034

Mr. P. Granville
Code 541
Naval Ship Research and Development Center
Washington, D.C. 20034

Mr. J.B. Hadler
Code 560
Naval Ship Research and Development Center
Washington, D.C. 20034

Dr. H.R. Chaplin
Code 600
Naval Ship Research and Development Center
Washington, D.C. 20034

Mr. G.H. Gleissner
Code 800
Naval Ship Research and Development Center
Washington, D.C. 20034

Dr. M. Strasberg
Code 901
Naval Ship Research and Development Center
Washington, D.C. 20034

Mr. J. McCarthy
Code 552
Naval Ship Research and Development Center
Washington, D.C. 20034

Code 03
Naval Air Systems Command
Washington, D.C. 20360

AIR 5301
Naval Air Systems Command
Department of the Navy
Washington, D.C. 20360

Code ORD 03
Naval Ordnance Systems Command
Washington, D.C. 20360

Code ORD 035
Naval Ordnance Systems Command
Washington, D.C. 20360

Code ORD 05413
Naval Ordnance Systems Command
Washington, D.C. 20360

Code ORD 9132
Naval Ordnance Systems Command
Washington, D.C. 20360

Oceanographer of the Navy
Washington, D.C. 20390

Commander
Naval Oceanographic Office
Washington, D.C. 20390

Chief Scientist (CNM PM-1)
Strategic Systems Project Office
Department of the Navy
Washington, D.C. 20360

Technical Division (CNM PM 11-20)
Deep Submergence Systems Project Office
Department of the Navy
Washington, D.C. 20360

Dr. A.L. Slafkosky
Scientific Advisor
Commandant of the Marine Corps (Code AX)
Washington, D.C. 20380

Librarian Station 5-2
Coast Guard Headquarters
NASSIF Building
400 7th Street, S.W.
Washington, D.C. 20591

Office of Research and Development
Maritime Administration
441 G. Street, N.W.
Washington, D.C. 20235

Division of Ship Design
Maritime Administration
441 G. Street, N.W.
Washington, D.C. 20235

National Science Foundation
Engineering Division
1800 G. Street, N.W.
Washington, D.C. 20550

Dr. G. Kulin
National Bureau of Standards
Washington, D.C. 20234

Science & Technology Division
Library of Congress
Washington, D.C. 20540

Chief of Research & Development
Office of Chief of Staff
Department of the Army
The Pentagon, Washington, D.C. 20310

Professor A. Thiruvengadam
Department of Mechanical Engineering
The Catholic University of America
Washington, D.C. 20017

Professor G. Birkhoff
Department of Mathematics
Harvard University
Cambridge, Massachusetts 02138

AIR 604
Naval Air Systems Command
Department of the Navy
Washington, D.C. 20360

Dr. A.S. Iberall, President
General Technical Services, Inc.
451 Penn Street
Yeadon, Pennsylvania 19050

Professor J.F. Kennedy, Director
Iowa Institute of Hydraulic Research
State University of Iowa
Iowa City, Iowa 52240

Professor L. Landweber
Iowa Institute of Hydraulic Research
State University of Iowa
Iowa City, Iowa 52240

Dr. Lee Segel
Department of Mathematics
Rensselaer Polytechnic Institute
Troy, New York 12180

Code 6101E
Naval Ship Engineering Center
Center Building
Prince George's Center
Hyattsville, Maryland 20782